Nitrous acid is a global driver of photochemistry in fresh wildfire plumes

N. Theys[1*], R. Volkamer[2,3,4**], J.-F. Müller[1], K. J. Zarzana[2], N. Kille[3,4], L. Clarisse[5], I. De Smedt[1], C. Lerot[1], H. Finkenzeller[2,3], F. Hendrick[1], T. K. Koenig[2,3], C. F. Lee[2,3], C. Knote[6], H. Yu[1], M. Van Roozendael[1]

[1] Royal Belgian Institute for Space Aeronomy (BIRA-IASB), Brussels, Belgium.

[2] Department of Chemistry, University of Colorado Boulder, Boulder, CO, USA.

[3] Cooperative Institute for Research in Environmental Sciences (CIRES), Boulder, CO, USA.

[4] Department of Atmospheric Sciences, University of Colorado Boulder, Boulder, CO, USA.

[5] Université libre de Bruxelles (ULB), Spectroscopy, Quantum Chemistry and Atmospheric Remote Sensing (SQUARES), C. P. 160/09, Brussels, Belgium.

[6]Meteorological Institute, LMU Munich, Munich, Germany.

*Corresponding author: N. Theys, Royal Belgian Institute for Space Aeronomy, Brussels, Belgium (theys@aeronomie.be).

**Corresponding author: R. Volkamer, University of Colorado Boulder, Boulder, CO, USA (rainer.volkamer@colorado.edu).

Nitrous acid (HONO) is an important precursor of the hydroxyl radical (OH), which controls the degradation of pollutants, greenhouse gases, and contributes to photochemical smog. Due to lack of wide scale measurements, pyrogenic HONO emissions are uncertain, and currently are missing in most global models. Exploiting observations of the TROPOMI/Sentinel-5 Precursor satellite sounder, we provide here the first global survey of atmospheric HONO that directly addresses the need for wide scale measurements above and downwind of wildfires. Large, unambiguous enhancements of HONO are consistently found in fresh wildfire plumes from major ecosystems worldwide (savanna, grasslands, shrubland, tropical- and extratropical forests). We derive averaged HONO/NO_2 enhancement ratios and show that these exhibit a strong and systematic dependence on biome type. Supported by aircraft measurements, we demonstrate that even the most recent assessments generally underestimate pyrogenic HONO emissions by a factor of two to four across all ecosystem types. At the observed levels, HONO photolysis accelerates oxidative plume chemistry that forms ozone and secondary organic aerosol, and is responsible for two-thirds of OH production in fresh wildfire plumes worldwide. Global model calculations indicate a potential substantial impact of pyrogenic HONO emissions on atmospheric composition, enhancing ozone levels by up to 7ppbv regionally.

As primary oxidant of the atmosphere, OH radicals control the degradation of pollutants and greenhouse gases, and contribute to photochemical smog and ozone formation[1]. HONO is a key constituent of the tropospheric photochemistry, primarily as a source of OH. However, the HONO budget remains poorly constrained[2], despite recent scientific progress[3-7].

Biomass burning (BB) plays an important role in the global emission budget of reactive gases in the atmosphere[8]. Fires can cause large perturbations to the chemistry and composition of the atmosphere, affecting climate and leading to adverse effects on human health. Atmospheric chemical transport models provide an ideal means of assessing these impacts, but require an accurate representation of the chemistry in fire plumes as well as reliable ecosystem dependent emission estimates that are usually based on fire activity data together with estimated emission factors obtained from laboratory and in situ measurements[9,10].

Global models that assess the importance of HONO as OH precursor on the global scale[11] typically neglect HONO from wildfires and thus provide lower limit estimates. Known formation mechanisms of HONO in fire plumes include direct emissions[12], heterogeneous conversion of NO_2 on organic aerosols[4,13] and on soot[3,14], photolysis of particulate nitrate[15], hydrolysis of NO_2 dimers boosted in the presence of ammonia[16]. However, the relative importance of these processes in fires and on the HONO to NO_x ($NO+NO_2$) emission factors have proven difficult to quantify, especially on large scales, due to the lack of representativeness of measurements performed in smoke chambers[17,18] or collected in situ[19-24], and also because of the short atmospheric lifetime of HONO. Global satellite sounders have revolutionized our knowledge on the emission mechanisms and global distributions of many short-lived gaseous pollutants[25-27].

HONO however, has hitherto been detected only once from space, namely in an exceptionally large stratospheric smoke plume[28] using the Infrared Atmospheric Sounder Interferometer (IASI). Here we show that the new satellite TROPOspheric Monitoring Instrument (TROPOMI), launched in 2017 onboard Sentinel-5 Precursor, is capable of observing HONO consistently in freshly emitted wildfire plumes, providing information that is otherwise unavailable. To achieve this, TROPOMI has two decisive advantages over its predecessors (such as the Ozone Monitoring Instrument, OMI), namely a high spatial resolution (3.5x7 km²) and a higher signal-to-noise ratio. Compared to infrared sounders, TROPOMI measures in the ultraviolet-visible domain and has a much better sensitivity to HONO in the lowermost atmosphere.

Global pyrogenic HONO probed from space

Daily global HONO slant column densities (SCD, or the integrated concentration along the light path) were retrieved from TROPOMI radiance spectra (Methods) using Differential Optical Absorption Spectroscopy[29,30] (DOAS). A typical example is shown in Fig. 1a for wildfires in British Columbia (Canada), along with unambiguous spectroscopic evidence for the presence of HONO in the selected TROPOMI observation (inset in Fig. 1a). Inspection of the daily HONO maps reveals consistent large local enhancements near the fire sources similar to enhancements of nitrogen dioxide (NO_2) SCD that are co-retrieved in the same wavelength range (Supplementary Fig. S1a). This suggests that HONO is either directly emitted from fires or very rapidly formed by pyrogenic precursors. The geographical extent of the observed HONO plumes is generally limited to a few tens of kilometers downwind of the fires, reflecting the short atmospheric lifetime of HONO (order of 15 minutes in clear air[31], longer in smoke plumes) and the rapidly changing conditions as the plumes age and dilute. We have analyzed one full year of global measurements between May 2018 and April 2019. Based on conservative selection criteria (Methods), we isolated a total of 5093 TROPOMI pixels with unambiguous HONO detection, all coinciding with wildfire plumes, as readily confirmed by TROPOMI-retrieved distribution of other pyrogenic compounds including carbon monoxide (CO), NO_2, formaldehyde (HCHO), glyoxal (CHOCHO), and aerosols (see examples in Supplementary Fig. S1). These HONO observations (Fig. 1b) are located over dominant BB regions, as evidenced from the data of GFED (Global Fire Emissions Database[32]; Supplementary Fig. S2a), allowing the first meaningful assessment of HONO emissions from fires in a global context.

Comparison with aircraft observations

The TROPOMI HONO measurements are corroborated by comparisons with aircraft HONO column observations acquired during the Biomass Burning Fluxes of Trace Gases and Aerosols (BB-FLUX) field study conducted in the US Pacific Northwest during the summer of 2018 wildfire season (Methods). Here we use measurements of the wildfire plume from the Rabbit Foot Fire, Idaho, on August 12, 2018. The aircraft, equipped with a zenith-sky DOAS instrument, flew under the smoke layer and performed two traverses of the plume, nearly synchronized with TROPOMI. HONO and NO_2 are retrieved using identical fit settings as used by the satellite. The HONO SCDs derived from the aircraft measurements provide independent corroborating evidence for the presence of HONO in large amounts at the same location as the satellite observations (Fig. 2a). Notably, the aircraft measurement integrates HONO and NO_2 over the entire wildfire plume, while the satellite measurement primarily samples the top layer of the plume (Supplementary Fig. S3). The higher HONO SCD measured from the aircraft reflects the fact that all photons that reach the plane have traversed the entire plume. For comparison with the satellite, we compare the enhancement ratios of the measured HONO SCD to the NO_2 SCD (RHN) to cancel differences in Air Mass Factors (AMFs) that arise from the different sampling geometries. The RHN cancellation of AMFs is justified because both gases are retrieved in the same wavelength range (Methods), as long as the HONO and NO_2 profile shapes in the plume are similar (see Supplement). Similar profile shapes are expected since both are photolabile species. Furthermore, the RHN is independent of the trace gas dilution during transport, and a useful metric[33,18] of the photochemical production rate of HONO.

Comparisons of TROPOMI and aircraft RHNs are presented in Figs. 2b and 2c. The satellite RHNs (0.33-0.54) agree very well with the aircraft values (0.29-0.54) after the data are aligned along a common plume age axis (Methods). There is no satellite bias discernible within the low (<10%) measurement error of the aircraft data. Two additional BB-FLUX research flights (Supplementary Fig. S4) show similarly good agreement over a wider range of RHN values, further supporting the assumption of similar HONO and NO_2 profile shapes inside the plume. The aircraft data reveals variability in RHN on fine spatial (few 100m) and temporal scales (seconds to minutes) that cannot be resolved from space. Notably, comparing aircraft column observations with columns from space actively bridges the different spatial scales to the best degree possible, though atmospheric variability remains a limiting factor. Overall, Fig. 2c and Supplementary Fig. S4 illustrates that the aircraft data approximate the satellite measured RHN best when near synchronous observations of similar plume ages are compared.

Uncertainties in HONO and NO_2 SCDs and RHN

No statistically significant bias in the satellite RHN is observed (6±8 %, Supplementary Table S1), reflecting identical HONO and NO_2 retrieval settings and cross-section spectra used for both aircraft and satellite (known to better 6% and 5%, Supplementary Table S1). However, a common systematic error cannot be fully excluded either. For TROPOMI global observations, the RHN systematic uncertainty is of ±25%. Contribution of SCDs random errors to biome averaged RHN values (as in Table 1 below) is negligible due to the large number of HONO detections. Furthermore, the RHN variability within a satellite ground pixel is found to be highly significant in the aircraft data, and similar to the variability between nearby satellite detections (Fig. 2c, and Supplementary Fig. S4). Interestingly, the satellite bias is insignificant also within the ±6.9%

uncertainty of the aircraft data (accuracy in RHN, excluding cross-sections errors). This suggests that plume heterogeneity is not limiting the comparison between both remote sensing platforms, and reflects the benefits of more direct comparison by sampling over extended spatial scales.

Enhanced HONO relative to NO_2 surveyed worldwide

In Figs. 2b and 2c, it is noteworthy that TROPOMI RHN significantly increases (to values as high as 1.2) for pixels near the fire sources. This feature is commonly observed for the fires globally, and is directly the result of elevated HONO SCDs (rather than low NO_2 SCDs) near the fires (Supplementary Fig. S5). This suggests that HONO primary emissions either dominate over secondary sources, or cannot easily be separated from fast secondary formation close to the fires. From the global detections, distinct spatial patterns of RHN clearly emerge (Fig. 3a) that are attributable to the distribution of ecosystems. Observed RHNs (10th-90th percentile) tend to be lower (0.14-0.61) over regions dominated by fires from grassland, savannas and open shrubland (Kazakhstan, most of Africa and Australia), intermediate values (0.23-0.62) are found over tropical deciduous forest fires (Central and South America, mainland Southeast Asia, the eastern coast of Australia, and east of Madagascar), and the highest values (0.32 -0.78) correspond to extra-tropical evergreen forest burns (USA, Canada and far Eastern Russia). This dependence of RHN on vegetation type matches findings of earlier studies (Table 1). However, the TROPOMI RHN is a factor of 2-4 higher compared to most values found in the current literature[10], regardless of the vegetation type. This is highly significant, and well outside the measurement uncertainty. Because of its detection limit, satellite data is more representative of large wildfires (Supplementary Fig. S2b) but the finding of high RHNs is robust over the complete range of fire emissions covered by TROPOMI HONO measurements (Supplementary Fig. S2c). For savanna fires, a statistically significant anti-correlation between the fire strength and RHN is observed, consistent with strong savanna fires emitting larger amounts of NO_x. Our results suggest that global HONO production from fires has been significantly underestimated, and we present several reasons for this. First, the published RHN estimates from field studies (see Supplementary Table S2) are based on in situ measurements most often for modest burns, optically thin BB plumes (thus very different than the fire emissions sampled by TROPOMI and BB-FLUX), and sampled away from the core of fire plumes. This is supported by recent in situ observations of high RHN in fresh plumes from large fires[35]. Second, the highly polluted conditions in sizeable fire plumes likely favor the conversion of NO_2 to HONO through heterogeneous processes[3,13,16] as well as NO_2 loss, for instance from peroxyacetyl nitrates (PANs) formation. These effects would be seen more in the distal rather than the proximal part of the plume, so that such a potential bias can only explain part of the observed discrepancy. Third, the higher RHNs derived from TROPOMI observations likely reflect the ability to sample freshly emitted, almost undiluted plumes inside the zone surrounding fires that is hardly accessible to research flights, because of fire-induced atmospheric turbulence, and/or due to temporary flight restriction (TFR) zones. A clear decrease is observed for RHN, HONO and NO_2 with increasing distance from the fires (Supplementary Fig. S5). This presents direct evidence for the difficulty of establishing emission factors for highly reactive species from field measurements downwind of fires in rapidly evolving plumes, whose composition changes on short temporal and spatial scales. Fourth, emission factors determined from smoke chamber experiments (Table 1) are obtained under specific atmospheric mixing and photochemical conditions that prevail in the laboratory settings, and that are likely different from the conditions found in actual wildfires (in terms of fuel heterogeneity, wind fields, humidity gradients, fire strength, fuel consumption rates, pyrolysis contributions, etc.). Consistent with this hypothesis, our evidence that RHN depends on fire strength of savanna fires (Supplementary Fig. S2c) corroborates previous findings[36] that burn conditions modify fire emissions.

HONO as the main source of OH in fresh smoke plumes

The importance of HONO for atmospheric chemistry in fire plumes is further demonstrated by contrasting the calculated production rates of OH due to HONO photolysis with the corresponding estimated production rates due to other known pyrogenic sources of OH, including the photolysis of ozone in presence of H_2O, the photolysis of 16 oxygenated volatile organic compounds (OVOCs), and the ozonolysis of 12 alkenes (Methods). Constrained by TROPOMI measurements, we estimate the relative contributions of the most important precursory compounds to the total OH production in fresh wildfire plumes worldwide, leveraging the fact that relative contributions are independent of assumptions about aerosol optical properties and plume optical thickness to first order (Methods). On average for all wildfire plumes detected by TROPOMI, the photolysis of HONO accounts for 63±16% of the total OH production, and more than 80% locally (Fig. 3b); the error bar accounts for uncertainties in the abundances of the contributing compounds and in their less rates and OH yields. The photolysis of all OVOCs accounts collectively for 35% (HCHO: 18%, CHOCHO: 4%, other OVOCs: 13%), and other sources for 3% (ozone photolysis: 1%, alkenes ozonolysis: 2%) of the total OH production from fires. The daytime contribution of HONO obtained here is much higher than previously reported (12-34%), for urban conditions[37, 38] and forest canopy[39]. This makes HONO the main precursor of OH in fresh fire plumes; this finding is supported on a local scale, by reported large OH production due to HONO from western US wildfires[35]. Under the simplifying assumption that pyrogenic HONO is directly emitted, its impact on other atmospheric compounds is also substantial. We estimate concentration enhancements of up to 30% for OH and 10% for O_3 with global model simulations (Supplementary Fig. S6). Pyrogenic HONO emissions also represent a significant input to the global NOx budget, estimated at ca. 1 TgN yr^{-1}.

We have demonstrated the first global HONO observations from space. The detailed study of further HONO observations – including from geostationary platforms – in connection with models and additional atmospheric and fire activity data, holds largely unexplored potential to provide valuable insights into the still poorly understood formation mechanisms of HONO, and its importance for atmospheric chemistry and climate in the global context of wildfires and possibly also urban air.

References

1. Finlayson-Pitts, B. J., Pitts, J. N. *Chemistry of the Upper and Lower Atmosphere: Theory, Experiments and Applications* (Academic Press, San Diego, 2000), first ed.
2. Spataro, F., Ianniello, A. Sources of atmospheric nitrous acid: State of the science, current research needs, and future prospects. *Journal of the Air & Waste Management Association*. **64**:11, 1232-1250 (2014).
3. Ammann, M. et al., Heterogeneous production of nitrous acid on soot in polluted air masses. *Nature*. **395**, 157–160 (1998).
4. Stemmler, K., Ammann, M., Donders, C., Kleffmann, J., George, C. Photosensitized reduction of nitrogen dioxide on humic acid as a source of nitrous acid. *Nature*. **440**, 195–198 (2006).
5. Zhou, X. et al. Nitric acid photolysis on forest canopy surface as a source for tropospheric nitrous acid. *Nat. Geosci*. **4**, 440–443 (2011).
6. Oswald, R. et al. HONO emissions from soil bacteria as a major source of atmospheric reactive nitrogen. *Science.* **341**, 1233–1235 (2013).
7. VandenBoer, T. C. et al. Nocturnal loss and daytime source of nitrous acid through reactive uptake and displacement. *Nat. Geosci*. **8**, 55-60 (2015).
8. Andreae, M. O., Merlet, P. Emissions of trace gases and aerosols from biomass burning. *Global Biogeochem. Cycles.* **15**, 955-966 (2001).
9. Akagi, S. K. et al. Emission factors for open and domestic biomass burning for use in atmospheric models. *Atmos. Chem. Phys.* **11**, 4039-4072 (2011).
10. Andreae, M. O. Emissions of trace gases and aerosols from biomass burning – An updated assessment. *Atmos. Chem. Phys.* **19***,* 8523-8546 (2019).
11. Elshorbany, Y. F. et al. Global and regional impacts of HONO on the chemical composition of clouds and aerosols. *Atmos. Chem. Phys.* **14***,* 1167-1184 (2014).
12. Veres, P. et al. Measurements of gas-phase inorganic and organic acids from biomass fires by negative-ion proton-transfer chemical-ionization mass spectrometry. *J. Geophys. Res.* **115**, D23302 (2010).
13. Nie, W. et al. Influence of biomass burning plumes on HONO chemistry in eastern China. *Atmos. Chem. Phys.* **15**, 1147-1159 (2015).
14. Monge, M. E. et al. Light changes the atmospheric reactivity of soot. *P. Natl. Acad. Sci. USA*. **107**, 6605–6609 (2010).
15. Ye, C., Zhang, N., Gao, H., Zhou, X. Photolysis of particulate nitrate as a source of HONO and NOx. *Environ. Sci. Technol.* **51** (12), 6849-6856 (2017).
16. Li, L. et al. Formation of HONO from the NH_3-promoted hydrolysis of NO_2-dimers in the atmosphere. *P. Natl. Acad. Sci. USA*. **115** (28), 7236-7241 (2018).

17. Keene, W. C. et al. Emissions of major gaseous and particulate species during experimental burns of southern African biomass. *J. Geophys. Res.* **111**, D04301 (2006).

18. Burling, I. R. et al. Laboratory measurements of trace gas emissions from biomass burning of fuel types from the southeastern and southwestern United States. *Atmos. Chem. Phys.* **10**, 11115-11130 (2010).
19. Trentmann, J. et al. An analysis of the chemical processes in the smoke plume from a savanna fire. *J. Geophys. Res.* **110**, D12301 (2005).
20. Yokelson, R. J. et al. The Tropical Forest and Fire Emissions Experiment: overview and airborne fire emission factor measurements. *Atmos. Chem. Phys.* **7**, 5175-5196 (2007).
21. Yokelson, R. J. et al. Emissions from biomass burning in the Yucatan. *Atmos. Chem. Phys.* **9**, 5785–5812 (2009).
22. Akagi, S. K. et al. Measurements of reactive trace gases and variable O_3 formation rates in some South Carolina biomass burning plumes. *Atmos. Chem. Phys.* 13, 1141-1165 (2013).
23. Müller, M. et al. In situ measurements and modeling of reactive trace gases in a small biomass burning plume. *Atmos. Chem. Phys.* **16**, 3813-3824 (2016).
24. Neuman, J. A. et al. HONO emission and production determined from airborne measurements over the Southeast U.S. *J. Geophys. Res. Atmos.* **121**, 9237–9250 (2016).
25. Beirle, S., Boersma, K. F., Platt, U., Lawrence, M. G., Wagner, T. Megacity emissions and lifetime of nitrogen oxides probed from space. *Science.* **333**, 1737-1739 (2011).
26. McLinden, C. A. et al. Space-based detection of missing sulfur dioxide sources of global air pollution. *Nat. Geosci*. **9**, 496–500 (2016).
27. Van Damme, M. et al. Industrial and agricultural ammonia point sources exposed. *Nature.* **564**, 99-103 (2018).
28. Clarisse, L., R'Honi, Y., Coheur, P.-F., Hurtmans, D., Clerbaux, C. Thermal infrared nadir observations of 24 atmospheric gases. *Geophys. Res. Lett.* **38**, L10802 (2011).
29. Platt, U., Perner, D., Harris, G. W., Winer, A. M., Pitts, J. N. Observations of nitrous acid in an urban atmosphere by differential optical absorption. *Nature.* **285**, 312-314 (1980).
30. Platt, U., Stutz, J. Differential Optical Absorption Spectroscopy (DOAS), Principle and Applications. ISBN 3-340-21193-4, Springer Verlag, Heidelberg (2008).
31. Hendrick, F. et al. Four years of ground-based MAX-DOAS observations of HONO and NO_2 in the Beijing area. *Atmos. Chem. Phys.*, **14**, 765–781 (2014).
32. van der Werf, G. R. et al. Global fire emissions estimates during 1997-2016. *Earth System Science Data*. **9**, 697-720 (2017).
33. Kleffmann, J. Daytime sources of nitrous acid (HONO) in the atmospheric boundary layer. *Chem. Phys. Chem.* **8**, 1137–1144 (2007).
34. Friedl, M. A. et al. MODIS Collection 5 global land cover: algorithm refinements and characterization of new datasets. *Remote Sens. Environ.* **114**, 168–182 (2010).
35. Peng, Q., et al. HONO Emissions from Western U.S. Wildfires Provide Dominant Radical Source in Fresh Wildfire Smoke. *Environ. Sci. Technol*. **54**, 5954-5963 (2020).
36. Liu, X. et al. Airborne measurements of western U.S. wildfire emissions: Comparison with prescribed burning and air quality implications. *J. Geophys. Res.-Atmos.* **112**, 6108-6129 (2017).

37. Alicke, B., Platt, U., Stutz, J. Impact of nitrous acid photolysis on the total hydroxyl radical budget during the Limitation of Oxidant Production/Pianura Padana Produzione di Ozono study in Milan. *J. Geophys. Res.-Atmos.* **107**, 8196 (2002).
38. Volkamer, R., Sheehy, P., Molina, L. T., Molina, M. J. Oxidative capacity of the Mexico City atmosphere – Part 1: A radical source perspective. *Atmos. Chem. Phys.* **10**, 6969-2991 (2010).

39. Kleffmann, J. et al. Daytime formation of nitrous acid: A major source of OH radicals in a forest. *Geophys. Res. Lett.* **32**, L05818 (2005).

METHODS

TROPOMI retrieval of HONO and NO_2

TROPOMI[40] is the single-payload of the Sentinel-5 Precursor platform launched in October 2017. It is a nadir-viewing remote sensing instrument measuring the solar radiation reflected by the Earth and backscattered by its atmosphere. TROPOMI has heritage from OMI [41] and the SCanning Imaging Absorption spectroMeter for Atmospheric CartograpHY[42] (SCIAMACHY). The instrument is a push-broom imaging spectrometer with eight spectral bands covering ultraviolet to shortwave infrared wavelengths with a spectral resolution of 0.25–1 nm and a spectral sampling ratio of 2.5–6.7. Flying in a low-Earth early afternoon polar orbit with a wide swath of 2600 km resulting in daily global coverage, it delivers vertically integrated abundances of key atmospheric constituents (O_3, NO_2, SO_2, HCHO, CHOCHO, CO, CH_4) complemented by cloud and aerosol information, at the resolution of 3.5x5.5 km^2 (from 6 August 2019) or 3.5x7 km^2 (this study, compared to 13x24 km^2 and 30x60 km^2, for OMI and SCIAMACHY, respectively).

For this work, we analyze ultraviolet-visible spectral data measured between 1 May 2018 and 30 April 2019, and solar zenith angles lower than 65°. The HONO slant column density (SCD, in molecules cm^{-2}) is retrieved from each recorded radiance spectrum using the established technique of Differential Optical Absorption Spectroscopy[30] (DOAS). In brief, the measured spectrum is modeled using a reference spectrum, absorption cross-sections of relevant trace gases, and radiance closure terms. The fitted parameters for the trace gases are the SCDs and represent the corresponding concentrations integrated along the mean optical light path in the atmosphere. Here the retrieval scheme is an adapted version of the TROPOMI HCHO algorithm[43]. We have followed recommended settings[44] and used a wavelength interval of 337–375 nm optimized for HONO (see details in Supplementary Table S3). In the same spectral fitting step, the slant column of NO_2 is retrieved. Given the relatively low peak-to-peak absorption of NO_2 in the ultraviolet, the noise on retrieved NO_2 SCDs is larger than in the visible range[45]. However, the signal is such that there is no difficulty to detect NO_2 in wildfire plumes. To determine enhanced NO_2 SCD for the fire plumes, a stratospheric NO_2 correction is applied, and is estimated using measurements at the same latitude from over a sector (see Supplementary Table S3) with negligible tropospheric NO_2 contribution[46].

Determination of the vertical column density (VCD, vertically integrated concentration) from the measured SCD requires radiative transfer simulations to derive air mass factors (AMF, where AMF=SCD/VCD). The AMF simulates the trace gas concentration integrated along the complex photon path in the plume, relative to the vertical path. Here, the AMF can be formulated[47] by:

$$AMF = \int bAMF\,(z).N(z).dz \qquad (1)$$

where N(z) is the normalized concentration profile of the trace gas of interest and bAMF is the height-resolved AMF (referred as box-AMF) that contains all dependences to parameters (wavelength, geometry, surface reflectance, clouds, aerosols, etc.) influencing the vertical sensitivity of the measurement, except N(z). In case of HONO and NO_2 from fires, a general AMF computation applicable globally is difficult because crucial input parameters are poorly known, notably the trace gases vertical distribution and the aerosol optical properties and extinction vertical profile (impacting bAMF).

We have calculated the ratio of HONO to NO_2, a proxy for HONO production, independent of the dilution of the trace gases during transport. Since NO_2 and HONO are jointly retrieved in the same spectral region, the box-AMFs can be considered identical for both species. Under the assumption that HONO and NO_2 have the same profile shapes (which is supported by our validation results, Fig. 2c), in first approximation, the AMFs of HONO and NO_2 are the same (Eq. 1). We can therefore formulate RHN independently of the error-prone AMFs:

$$RHN = VCD_{HONO}/VCD_{NO2,corr} \approx SCD_{HONO}/SCD_{NO2,corr} \quad (2)$$

where SCD_{HONO} is the HONO SCD, $SCD_{NO2,corr}=SCD_{NO2}–SCD_{NO2,strato}$ is the retrieved NO_2 SCD (SCD_{NO2}) corrected for its stratospheric contribution ($SCD_{NO2,strato}$). An error budget on SCDs and RHN is given in Supplementary Table S1. In particular, the estimated RHN error from imperfect cancellation of AMFs (due to wavelength dependence) is less than ~1%.

For a quantitative comparison of the TROPOMI RHN, nearly synchronized aircraft remote-sensing observations of HONO and NO_2 SCDs were used (see below). Conversely, the comparison of TROPOMI column-based RHN with aircraft in situ concentration RHN measurements is not considered here, as it is unlikely to carry much meaning, given the inhomogeneity of HONO and the fundamental difference in air mass sampling of the two techniques.

To identify global HONO plumes and study source regions in a systematic and consistent way, a set of criteria was formulated that can be satisfactorily applied globally without the need for external fire data sources. Cloud information is not used either as it could lead to statistical bias, for example by filtering pyrocumulus clouds. After removing obvious outliers (based on fitting residuals), a detection test is applied: first, only satellite data over land are considered. Secondly, satellite data are kept when $SCD_{HONO}>3xSCDE_{HONO}$ (where $SCDE_{HONO}$ is the HONO SCD uncertainty from the fit) and if at least one neighboring pixel satisfies the same criterion. An additional selection of the pixels with $SCD_{NO2,corr}>3xSCDE_{NO2}$ (where $SCDE_{NO2}$ is the NO_2 SCD uncertainty from the fit) is also applied, to improve the selectivity of wildfire plumes and to stabilize RHN. However, the resulting pixels selection leads to elevated false HONO detections over regions with large anthropogenic NO_2 signal. Therefore, a final and conservative selection criterion on $SCD_{HONO}>4x10^{15}$ molecules.cm^{-2} is used to retain only the unambiguous pyrogenic HONO detections. Applying these rather strict criteria to one year of TROPOMI data yields a set of 5093 usable HONO ground pixel detections, all located over biomass burning areas, giving additional confidence in the selection approach.

Aircraft measurements

The Biomass Burning Fluxes of Trace Gases and Aerosol (BB-FLUX) field campaign took place during the summer of 2018 wildfire season in the Pacific Northwest around Boise, ID, USA. The University of Wyoming King Air research aircraft was equipped with remote sensing and in situ instruments, including the University of Colorado Zenith Sky DOAS (CU ZS-DOAS) instrument, which performed measurements of NO_2, HONO, HCHO and CHOCHO using scattered solar photons in the zenith geometry. The aircraft was deployed underneath, inside and above the wildfire plumes to measure column enhancements, wind speed, and plume vertical structure. HONO and NO_2 differential SCDs were retrieved using the same fit settings as TROPOMI (Supplementary Table S3). The background on either side of the plume was linearly interpolated, and subtracted to derive trace gas SCD enhancements inside the plume. A total of 37 research flights (RFs) were conducted, studying wildfires in Idaho, California, Oregon, Nevada, Utah and Washington. A small subset of the BB-FLUX flights actively coordinated locating the plane below/near wildfire plumes at the TROPOMI overpass times. In particular, BB-FLUX RF11 on 12 August 2018 targeted the Rabbit Foot Fire in central Idaho close in time to the S5P overpass (~20:45 UTC). The aircraft conducted two plume underpasses between 20:00 and 20:15 UTC 50 km downwind of the fire. Two additional flights were used for comparison with TROPOMI, BB-FLUX RF13 on 15 August 2018 for the same Rabbit Foot Fire, and BB-FLUX RF15 on 19 August 2019 over the Watson Creek Fire (Oregon). For the two flights, the aircraft traverses sampled the wildfire plume at the S5P overpass time ±15 minutes.

Although the satellite and aircraft HONO SCDs presented in this study agree well qualitatively, a thorough comparison is not straightforward because of differences in spatial-temporal sampling of the air masses sounded by the two instruments, which have very different fields of view. Furthermore, because of different observation geometries, the retrievals have different sensitivity (light penetration) in the respective atmospheric vertical layers, in particular for large aerosol optical depths. We have estimated this effect using the radiative transfer model LIDORT[48] version 2.7. A set of AMFs were calculated at a wavelength of 355 nm for typical BB plumes. Because HONO (or NO_2) and aerosols are co-emitted, their vertical profiles were assumed to have the same shape modelled by a Gaussian peaking at 2km above the surface, with full width at half maximum of 0.5km. Biomass burning aerosols were represented by a bi-modal log-normal particles size distribution[49], with a single scattering albedo between 0.8 and 0.9, indicative of fresh to aged BB aerosols. Supplementary Fig. S3 shows an example of the dependence of the AMFs with aerosol optical depths (AOD). It illustrates the expected change in measurement sensitivity due to aerosols[50] and the inherent differences of AMF between aircraft and satellite measurements.

To evaluate the TROPOMI RHN estimates, we have calculated RHN from the aircraft HONO and NO_2 SCDs data, for NO_2 background corrected SCDs larger than 5×10^{15} molecules.cm^{-2}. An error analysis of SCDs and RHN is given in Supplementary Table S1. The advantages of comparing RHNs are that they do not vary with the AMFs, and that RHN is independent of the horizontal resolution. However, a time difference exists between aircraft and TROPOMI measurements (30-45 minutes in case of RF11, less than 15 minutes for RF13 and RF15), and a time adjustment is needed when comparing the aircraft and satellite RHNs. For this, we have estimated the age of the plume separately for the aircraft and TROPOMI measurements, using trajectory calculations made with the FLEXPART-WRF[51] model. The Global Fire Assimilation System of the Copernicus Atmosphere Monitoring Service[52] (CAMS GFAS) was used for fire locations, plume injection heights and emitted amounts. We released around 1×10^5 'particles' from each fire location and followed each particle on its path through the atmosphere, tracking the time since its release. Processes like turbulence were allowed to act stochastically on each particle to modify its trajectory. Our dispersion calculations result in plume age spectra for each model grid box, which we then sampled along the flight path of the aircraft and the locations of the TROPOMI measurements. The mass-weighted mean of the age spectrum is used as best-guess for plume age; its standard deviation allows to identify contamination by the Goldstone fire downwind (Fig. 2), and the corresponding data were removed from the analysis. At the edges of the plume, the estimated plume age was sometimes found unrealistic due to very low particles concentrations, and the respective data were not considered in the comparison. In total, seven TROPOMI pixels (out of 40) were filtered out in Fig. 2c.

Calculation of OH production rates

The OH production rates were calculated for every TROPOMI pixel where HONO was detected, using model-estimated photolysis rates. The sources of OH considered include photolysis of HONO, O_3 and oxygenated VOCs, and ozonolysis of alkenes. HONO, HCHO and CHOCHO mixing ratios were based on TROPOMI retrievals while concentrations of other VOCs were estimated from TROPOMI-derived HCHO and enhancement ratios (Δ(VOC)/Δ(HCHO)) based on field data. The calculation of concentrations requires assumptions on vertical profiles of the constituents and AMFs (see below). Since these parameters are very uncertain (Supplementary Fig. S3), large uncertainties in OH production rates are expected; however, these assumptions have little impact on the relative contribution of HONO to the total OH production rate presented here, as the vertical profiles of HONO and pyrogenic VOCs are expected to be very similar in the BB plumes.

The concentrations of HONO, HCHO and CHOCHO at the assumed plume peak altitude of 2km were estimated from TROPOMI measurements of these compounds, using the fixed vertical profile described above. The corresponding HCHO and CHOCHO SCDs (see example maps in Supplementary Fig. S1) are extracted from the TROPOMI HCHO offline product[43] and the scientific TROPOMI CHOCHO product (adapted from GOME-2 CHOCHO retrievals[53]). Details on the DOAS settings are provided in Supplementary Table S3. The calculations were performed for an assumed AMF of 0.5 for HONO and HCHO. An AMF of 1 is used for CHOCHO as radiative transfer test simulations (described above) demonstrated twice the measurement sensitivity in the visible part of the spectrum (where glyoxal is retrieved) than in the ultraviolet. The estimated uncertainty on HCHO concentrations (relative to those of HONO) is ca. 27%, resulting from an SCD uncertainty[43] of 10% and AMF errors related to differences in vertical profiles (20%) and in the wavelength ranges of the retrievals (15%), based on radiative transfer model sensitivity calculations. The CHOCHO concentration uncertainty (30%) is assumed to be similar to that of HCHO.

The photolysis rates were obtained from the MAGRITTE chemistry-transport model[54,55], which relies on the TUV photorate calculation package[56] with meteorological and other fields (pressure, temperature, surface downward solar radiation, total ozone columns) derived from ECMWF ERA-Interim reanalyses[57]. Potential misrepresentation of the effects of clouds and aerosols might lead to significant uncertainties in the photorates, but with little influence on their relative magnitudes and therefore on the relative contributions of the different photolytic processes. The uncertainty of the relative contribution of non-photolytic processes (alkene ozonolysis) is increased due to these effects, by an assumed factor of 2, with very little impact on the overall uncertainty of HONO contribution.

A constant ozone mixing ratio of 50 ppbv was assumed, whereas H_2O and temperature were obtained from ECMWF. Uncertainties in O_3 and H_2O are significant but have little bearing on the conclusions, as O_3 photolysis and alkene ozonolysis contribute for only a few percent of the total OH source.

Besides OH formation due to HONO and O_3 photolysis, the photolysis of organic compounds (primarily carbonyls) and the ozonolysis of alkenes generate OH radicals as well as HO_2 and RO_2 radicals which are partially converted to OH, depending on photochemical conditions[38]. Biomass burning plumes are usually characterized by high NOx levels, typically in the ppbv range[58]. In the TROPOMI pixels where HONO has been detected and quantified, the estimated median NO_2 volume mixing ratio is ~25 ppbv at the peak of the plume, when assuming an AMF of 0.5. Adopting an NO/NO_2 ratio of 0.2, based on airborne measurements in BB plumes during the ARCTAS campaign over boreal forests[59,60], the resulting NO concentrations (~5 ppbv) are such that HO_2 radicals produced in the plume are almost completely (>99%) converted to OH. The same applies to non-acyl RO_2 radicals, converted to HO_2 and then OH. For acylperoxy radicals (ACO3), however, formation of PAN-like compounds through ACO3+NO_2 is dominant, and only ~30% of these radicals are converted to OH, based on reported rates[61] for ACO3+NO and ACO3+NO_2 (for lower tropospheric conditions and NO/NO_2=0.2).

The VOC photolysis processes considered here are listed in Supplementary Table S4 along with their corresponding OH yield, assuming conversion efficiencies of 100% for HO_2 and for non-acyl peroxys, and 30% for acylperoxy radicals. These yields are based on the Master Chemical Mechanism[62,63] (MCM) v3.3.1 (http://mcm.leeds.ac.uk/MCM). The photorates (relative from that of HCHO) were estimated using TUV, with photolysis parameters from MCM. For furfural, the OH yield is assumed, and the photorate was calculated using published absorption cross sections[64] and a quantum yield[65] of 0.01, of the same order as for methacrolein and methylvinylketone[66].

The alkene ozonolysis processes considered here are listed in Supplementary Table S5 along with their reaction rate and estimated OH yield, under the same assumptions as above. The reaction rates and products are obtained from MCM v3.3.1. Monoterpenes are speciated as 25% α-pinene and 75% β-pinene based on measurements in BB plumes during ARCTAS[59]. The Supplementary Table S5 also provides the estimated OH production due to the reaction ($P_{OH}(VOC+O_3)$) for a given amount of the VOC (1 ppbv) and 50 ppbv O_3.

As noted above, the HCHO and CHOCHO concentrations were constrained by TROPOMI observations. The concentrations of the other pyrogenic VOCs were estimated using VOC/HCHO enhancement ratios (Supplementary Table S6) obtained from the review of emission factors[10]. The enhancement ratio of two compounds is defined as the ratio of the excess concentrations of the two compounds in the fire plume, relative to their ambient background concentrations. Enhancement ratios relative to CO or CO_2 are routinely used to estimate biomass burning emission factors[8] (in g per kg dry matter). Here the molar enhancement ratios relative to HCHO are calculated as $ER(VOC) = (EF(VOC)/MW_{VOC})/(EF(HCHO)/MW_{HCHO})$, where EF denotes the emission factor ($g.kg^{-1}$) and MW denotes molecular weight ($g.mole^{-1}$). Note that the natural variability of emission rates and the role of secondary chemistry (chemical production and losses within the plume) imply a large variability of enhancement ratios; in particular, the ratios depend on plume age and photochemical conditions. Furthermore, many minor oxygenated VOCs are either not measured or have so far unknown impacts due to lack of mechanistic information (e.g. furfurals).

Supplementary Table S7 gives the estimated contributions of VOC photolysis reactions to the production of OH, relative to the contribution of HCHO, as well as their estimated uncertainties. Those relative contributions are calculated as:

$$P_{OH}(VOC)/P_{OH}(HCHO)= (\Delta VOC/\Delta HCHO) \times J_{VOC}/J_{HCHO} \times Y_{OH}(VOC)/Y_{OH}(HCHO) \quad (3)$$

where the enhancement ratios (ΔVOC/ΔHCHO) are given in Supplementary Table S6, and the photolysis rates and OH yields are given in Supplementary Table S5. Although there is some variation between VOC enhancement ratios according to fire type (extratropical forest, temperate forest, tropical forest, savanna), the combined contribution of all VOC+hν reactions (besides HCHO+hν) is relatively uniform across fire types, and is of the same order as that of

HCHO. When excluding the contribution of HCHO and CHOCHO (for which TROPOMI retrievals are available), the contribution of VOC+hv can be approximated as 75±66% of the HCHO+hv contribution. The main contributing species are, besides HCHO and CHOCHO, methylglyoxal and biacetyl. Each of those two compounds contributes ~15-40% relative to formaldehyde.

Supplementary Table S8 provides the contribution of alkene ozonolysis to OH production, for given levels of O_3 and HCHO in the plume, calculated as the product of the enhancement ratio (Supplementary Table S6) by P_{OH} (Supplementary Table S5). The total production of OH due to alkene ozonolysis is highest for temperate and boreal forest fires, due to their high emissions of monoterpenes. Based on these results, the OH production rate per ppbv of HCHO is taken equal to 23±17 pptv.h^{-1} in Tropical regions, and 42±62 pptv.h^{-1} elsewhere, in the calculation of the overall OH production rate in TROPOMI pixels.

Modelled global impact of pyrogenic HONO

MAGRITTE v1.1[55] was run at 1°×1° resolution to estimate the impact of pyrogenic HONO on global composition during summer 2018. Meteorology is obtained from ECMWF ERA-Interim. The model includes a detailed representation of biogenic and pyrogenic VOC oxidation[67,55]. The photolysis rate calculation relies on TUV, with daily aerosol optical depth distributions from CAMS (https://ads.atmosphere.copernicus.eu). Biomass burning emissions are calculated based on GFED4[32] (van der Werf, 2017) with emission factors from recent assessment[10].

Two 6-month runs (March-August) were conducted, with and without pyrogenic HONO. Gas-phase HONO formation and loss are included in both simulations. The pyrogenic HONO emission factors are 1.10, 1.36, 2.29 g per kg of dry matter for savanna, tropical forest and extra-tropical forest fires, respectively, based on the RHN from Table 1 and NO_x emission factors[10], the NO/NO_2 ratio being taken equal to 0.2 (see above).

References

40. Veefkind, J. P. et al. TROPOMI on the ESA Sentinel-5 Precursor: A GMES mission for global observations of the atmospheric composition for climate, air quality and ozone layer applications. *Remote Sensing of Environment*. **120**, 70-83 (2012).
41. Levelt, P. F. et al. The Ozone Monitoring Instrument. *IEEE Trans. Geo. Rem. Sens.* **44**(5), 1093-1101 (2006).
42. Bovensmann, H. et al. SCIAMACHY: Mission objectives and measurement modes. *Journal of the Atmospheric Sciences*. **56**(2), 127–150 (1999).
43. De Smedt, I. et al. Algorithm Theoretical Baseline for formaldehyde retrievals from S5P TROPOMI and from the QA4ECV project. *Atmos. Meas. Tech.* **11**, 2395-2426 (2018).
44. Wang, Y. et al. MAX-DOAS measurements of HONO slant column densities during the MAD-CAT campaign: inter-comparison, sensitivity studies on spectral analysis settings, and error budget. *Atmos. Meas. Tech.* **10**, 3719-3742 (2017).
45. Behrens, L. K. et al. GOME-2A retrievals of tropospheric NO2 in different spectral ranges – influence of penetration depth. *Atmos. Meas. Tech.* **11**, 2769-2795 (2018).
46. Richter, A., Burrows, J. P. Retrieval of tropospheric NO2 from GOME measurements. *Adv. Space Res.* **29**, 1673–1683 (2002).
47. Palmer, P. I. et al. Air mass factor formulation for spectroscopic measurements from satellites: Application to formaldehyde retrievals from the Global Ozone Monitoring Experiment. *J. Geophys. Res.* **106**, 14539–14550 (2001).
48. Spurr, R. J. VLIDORT: A linearized pseudo-spherical vector discrete ordinate radiative transfer code for forward model and retrieval studies in multilayer multiple scattering media. *J. Quant. Spectrosc. Rad.* **102**, 316–342 (2006).
49. Wang, P., Tuinder, O. N. E., Tilstra, L.G., de Graaf, M., Stammes, P. Interpretation of FRESCO cloud retrievals in case of absorbing aerosol events. *Atmos. Chem. Phys.* **12**, 9057-9077 (2012).
50. Leitão, J. et al. On the improvement of NO_2 satellite retrievals – aerosol impact on the airmass factors. *Atmos. Meas. Tech.* **3**, 475-493 (2010).
51. Brioude, J. et al. The Lagrangian particle dispersion model FLEXPART-WRF version 3.1. *Geosci. Model Dev.* **6**, 1889–1904 (2013).
52. Kaiser, J. W. et al. Biomass burning emissions estimated with a global fire assimilation system based on observed fire radiative power. *Biogeosciences* **9**, 527–554 (2012).
53. Lerot, C., Stavrakou, T., De Smedt, I., Müller, J.-F., Van Roozendael, M. Glyoxal vertical columns from GOME-2 backscattered light measurements and comparisons with a global model. *Atmos. Chem. Phys.* **10**, 12059-12072 (2010).
54. Stavrakou, T. et al. Impact of short-term climate variability on volatile organic compounds emissions assessed using OMI satellite formaldehyde observations. *Geophys. Res. Lett.* **45**, 1621-1629 (2018).
55. Müller, J.-F., Stavrakou, T., Peeters, J. Chemistry and deposition in the Model of Atmospheric composition at Global and Regional scales using Inversion Techniques for Trace gas Emissions (MAGRITTEv1.0) - Part 1: Chemical mechanism. *Geosci. Model Dev.* **12**, 2307-2356 (2019).

56. Madronich, S. UV radiation in the natural and perturbed atmosphere, in Environmental Effects of Ultraviolet Radiation, edited by: Tevini, M., 17-69, Lewis, Boca Raton, Florida (1993).
57. Dee, D. P. et al. The ERA-Interim reanalysis: configuration and performance of the data assimilation system. *Q. J. R. Meteorol. Soc*. **137**, 553-597 (2011).
58. Trentmann, J., Andreae, M. O., Graf, H.-F. Chemical processes in a young biomass-burning plume. *J. Geophys. Res.* **108**, 4705 (2003).
59. Jacob, D. J. et al. The Arctic Research of the Composition of the Troposphere from Aircraft and Satellites (ARCTAS) mission: design, execution, and first results. *Atmos. Chem. Phys.* **10**, 5191-5212 (2010).
60. Simpson, I. J. et al. Boreal forest fire emissions in fresh Canadian smoke plumes: C1-C10 volatile organic compounds (VOCs), CO_2, CO, NO_2, NO, HCN and CH_3CN. *Atmos. Chem. Phys.* **11**, 6445-6463 (2011).
61. Atkinson R., et al. Evaluated kinetic and photochemical data for atmospheric chemistry: Volume II – gas phase reactions of organic species. *Atmos. Chem. Phys.* **6**, 3625-4055 (2006).
62. Saunders, S. M., Jenkin, M. E., Derwent, R. G., Pilling, M. J. Protocol for the development of the Master Chemical Mechanis, MCM v3 (Part A): tropospheric degradation of non-aromatic volatile organic compounds. *Atmos. Chem. Phys.* **3**, 161-180 (2003).
63. Jenkin, M. E., Young, J. C., Rickard, A. R. The MCM v3.3.1 degradation scheme for isoprene. *Atmos. Chem. Phys.* **15**, 11433-11459 (2015).
64. Colmenar, I. et al. UV absorption cross sections between 290 and 280 of a series of furanaldehydes: Estimation of their photolysis lifetimes. *Atmos. Environ.* **103**, 1-6 (2015).
65. Gandini, A., Parsons, J. M., Back, R. A. The photochemistry of 2-furaldehyde vapour. II. Photodecomposition: direct photolysis at 253.7 and 313 nm and Hg($^3P_1$)-sensitized decomposition. *Can. J. Chem.* **54**, 3095-3101 (1976).
66. Burkholder, J. B. et al. Chemical Kinetics and Photochemical Data for Use in Atmospheric Studies. Jet Propulsion Laboratory (JPL), California Institute of Technology, Pasadena, California. http://jpldataeval.jpl.nasa.gov (2015).
67. Stavrakou, T. et al. Evaluating the performance of pyrogenic and biogenic emission inventories against one decade of space-based formaldehyde columns. *Atmos. Chem. Phys.* **9**, 1037-1060 (2009).

Acknowledgments

This work has been performed in the frame of the TROPOMI and the BB-FLUX projects. We acknowledge financial support from ESA S5P MPC (4000117151/16/I-LG), Belgium Prodex TRACE-S5P (PEA 4000105598) projects. The BB-FLUX project is supported by the US National Science Foundation award AGS-1754019 (PI: R.V.). C.F.L. received summer support from the Department of Chemistry, CU Boulder. H.F. is recipient of a NASA graduate fellowship. L.C. is a research associate supported by the Belgian F.R.S.-FNRS. This paper contains modified Copernicus data (2018/2019) processed by BIRA-IASB. We wish to thank Trissevgeni Stavrakou for her advices on the model simulations. We acknowledge the open access policy of the GFED4 database. We thank the entire BB-FLUX science team, the pilots, and UW Flight center staff. The plume age estimates contain modified Copernicus Atmosphere Monitoring Service Information 2019. Neither the European Commission nor ECMWF is responsible for any use that may be made of the information it contains.

Author contributions

N.T., R.V., J.-F. M. designed research, M.V. supervised the work. N.T, I.D., C.L., H.Y., M.V. developed the satellite algorithms and processed the data. K.J.Z., N.K., H.F., T.K.K., C.F.L., R.V performed aircraft measurements and data analysis. J.-F. M., C.K. performed model calculations. All authors contributed to the text and interpretation of the results. N.T. analyzed and interpreted the TROPOMI HONO data, with the help of R.V. and K.J.Z. N.T. prepared all figures and wrote the manuscript, with input from all coauthors.

Competing interests

The authors declare no competing interests.

Additional information

Supplementary information accompanies this paper.

Data availability

The global data and validation data that support the findings of this study are available in the BIRA-IASB Data Repository (http://repository.aeronomie.be) with the identifier doi (tbd).

The TROPOMI HONO dataset used in this study is available from the corresponding author upon request.

The BB-FLUX dataset is available on request and should be cited with the following reference: Rainer Volkamer, Natalie Kille, Christopher F. Lee, Kyle J. Zarzana, Theodore K. Koenig, Benjamin Howard, Christoph Knote, Teresa Campos, Larry Oolman, Dave Plummer, Min Deng, Zhien Wang, Ravan Ahmadov, Brad Pierce, Florian Obersteiner, and Andreas Zahn, 2019; BB-FLUX: Biomass Burning Fluxes of Trace Gases and Aerosols. University of Wyoming - Research Flight Center, Laramie, WY. http://flights.uwyo.edu/projects/bbflux18/

Code availability

The DOAS code used to generate the satellite and aircraft data can be accessed at: http://uv-vis.aeronomie.be/software/QDOAS/index.php

The chemical mechanism of the MAGRITTE model used in this study can be obtained at: https://tropo.aeronomie.be/index.php/models/magritte

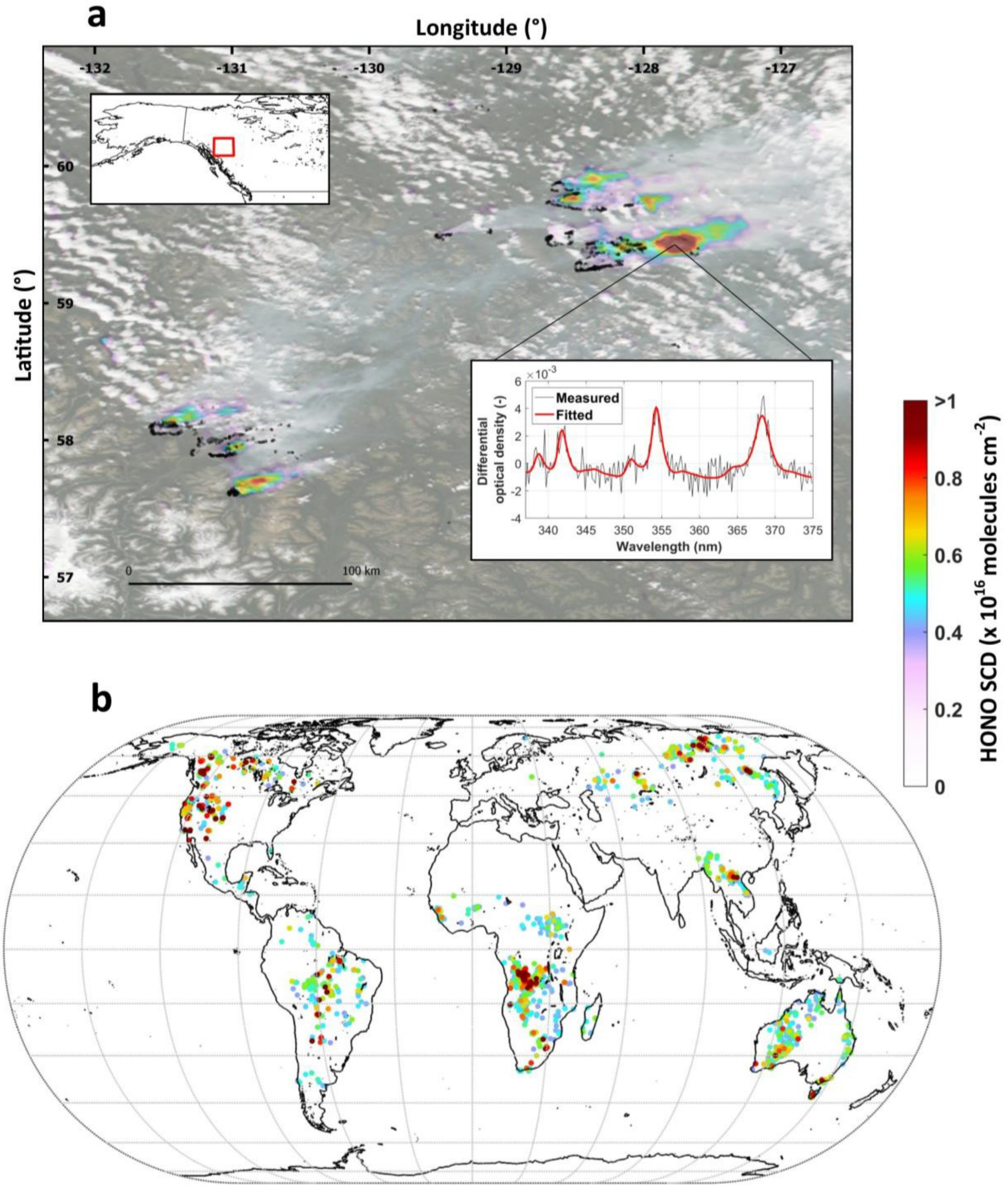

Fig.1 | Detection of HONO in wildfire plumes by TROPOMI. **a,** Example map of HONO slant column densities for wildfires in British Columbia on 21 August 2018. The background layer is a composite of true-color RGB image with fires detection and thermal anomalies product (black points) from VIIRS/Suomi-NPP instrument (source: https://worldview.earthdata.nasa.gov/), showing smoke aerosols and the fires source locations. The inset figure is the spectral proof of the HONO detection in the satellite pixel centered at 59.45°N, 127.82°W, illustrating the presence of the HONO differential absorption in the measured spectrum. **b**, Global map of HONO SCD detections (see Methods) for one year of TROPOMI measurements.

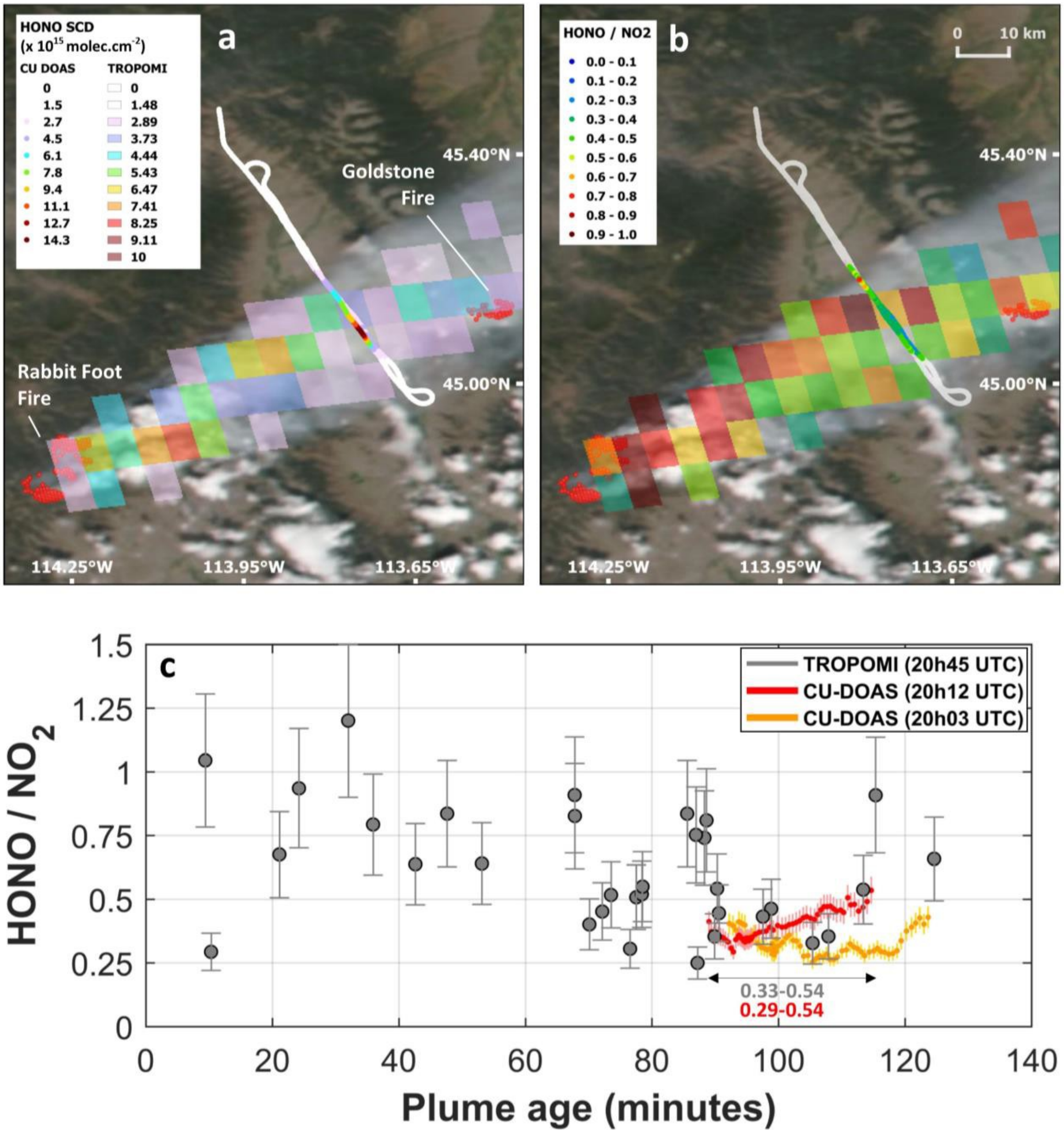

Fig. 2 | Comparison between TROPOMI and aircraft (CU-DOAS) measurements of the Rabbit Foot Fire (Idaho, USA) on August 12, 2018. a, HONO slant columns from TROPOMI (rectangles) and aircraft CU-DOAS (dots). The color scales best represent the ranges of observed values. **b**, RHN for measurements with unambiguous detection of HONO and NO_2. The background image for (**a-b**) shows biomass burning aerosols and the fires source locations (same data source as Fig. 1a). **c**, Comparison between TROPOMI and aircraft RHN as function of plume age (Methods). The two aircraft traverses of the plume are plotted separately. The ranges of RHN from TROPOMI and CU-DOAS are given over the intersection plume age interval (double arrow), for the traverse closest in time to the satellite. Error bars correspond to systematic uncertainties on RHNs.

Table 1. RHNs reported in the literature (Supplementary Table S2) and in this study, for different types of biomass burning. The TROPOMI results are classified using MODIS land cover type[34].

	Savanna, grassland, shrubland	Tropical forest	Extra-tropical forest
Field measurements	0.05 – 0.10	0.17 – 0.22	0.06 – 0.41 (0.86 [δ])
Laboratory experiments	0.05 – 0.19	0.17	0.13 – 0.20
This study*: average ± error*	**0.34±0.08**	**0.41±0.09**	**0.54±0.12**

[δ] Fresh smoke from large wildfires[35].

* Mean values for satellite HONO detections, mostly representative of fires with carbon emissions of 0.5 - 500 gC/m^2/month (Supplementary Fig S2b).

** Systematic uncertainty

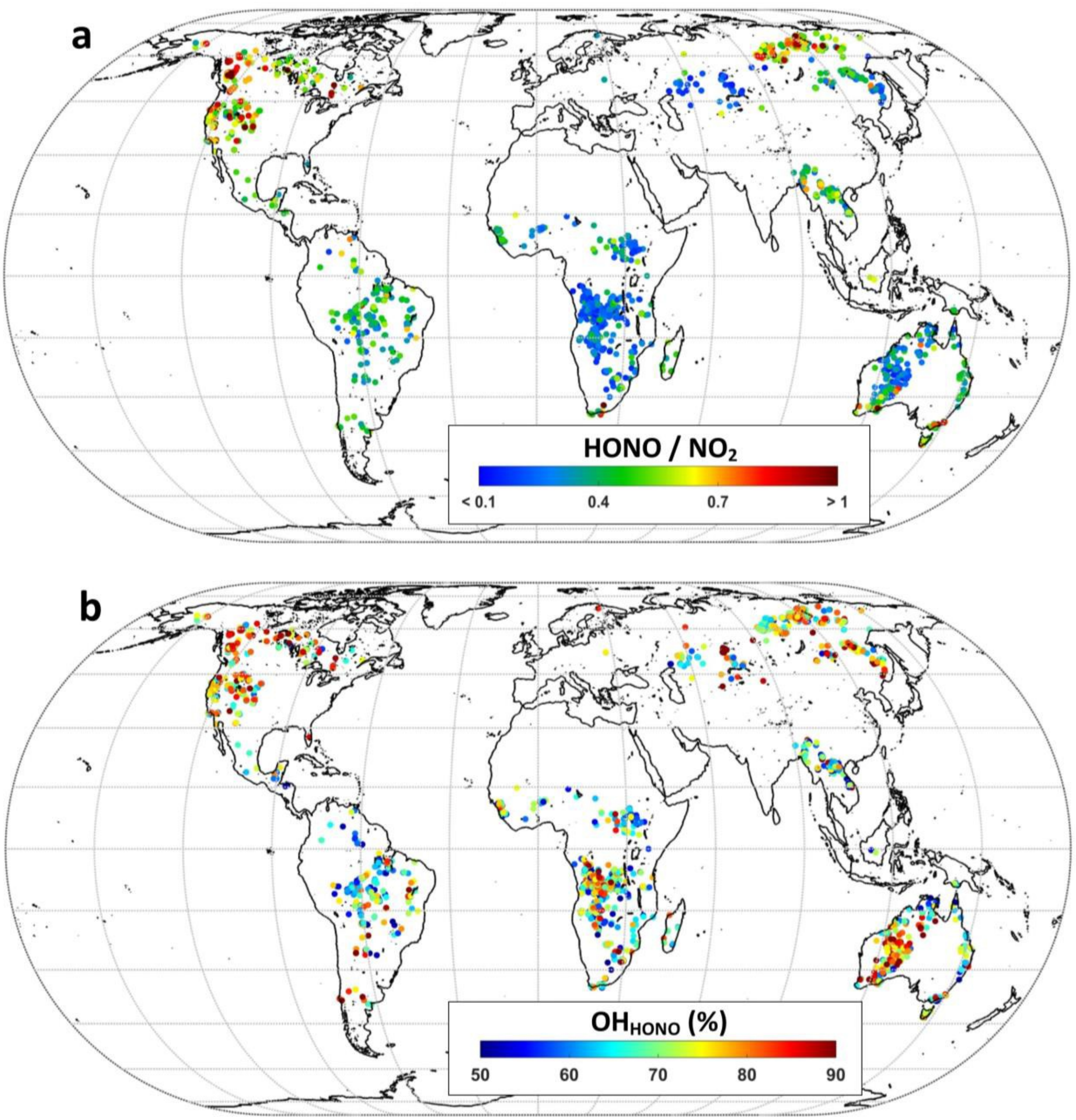

Fig. 3 | Satellite-derived RHN and relative production rate of OH due to HONO photolysis for fires emissions. a, RHN for one year of TROPOMI measurements (May 2018 - April 2019). The coloured symbols correspond to individual HONO detections (same as Fig. 1b). **b**, Satellite estimates of OH production (in percent) from HONO fire emissions. The OH production is calculated from HONO concentrations derived from the satellite detections (as (**a**)), assuming a single air mass factor and a fixed HONO concentration profile shape (Methods).

Supplementary Information contains Figures S1-S6, Tables S1-S8, two data files in the form excel sheets for global compilation of HONO detections for one year of TROPOMI measurements, and TROPOMI and aircraft data for the Rabbit Foot fire validation case, and supplementary references.

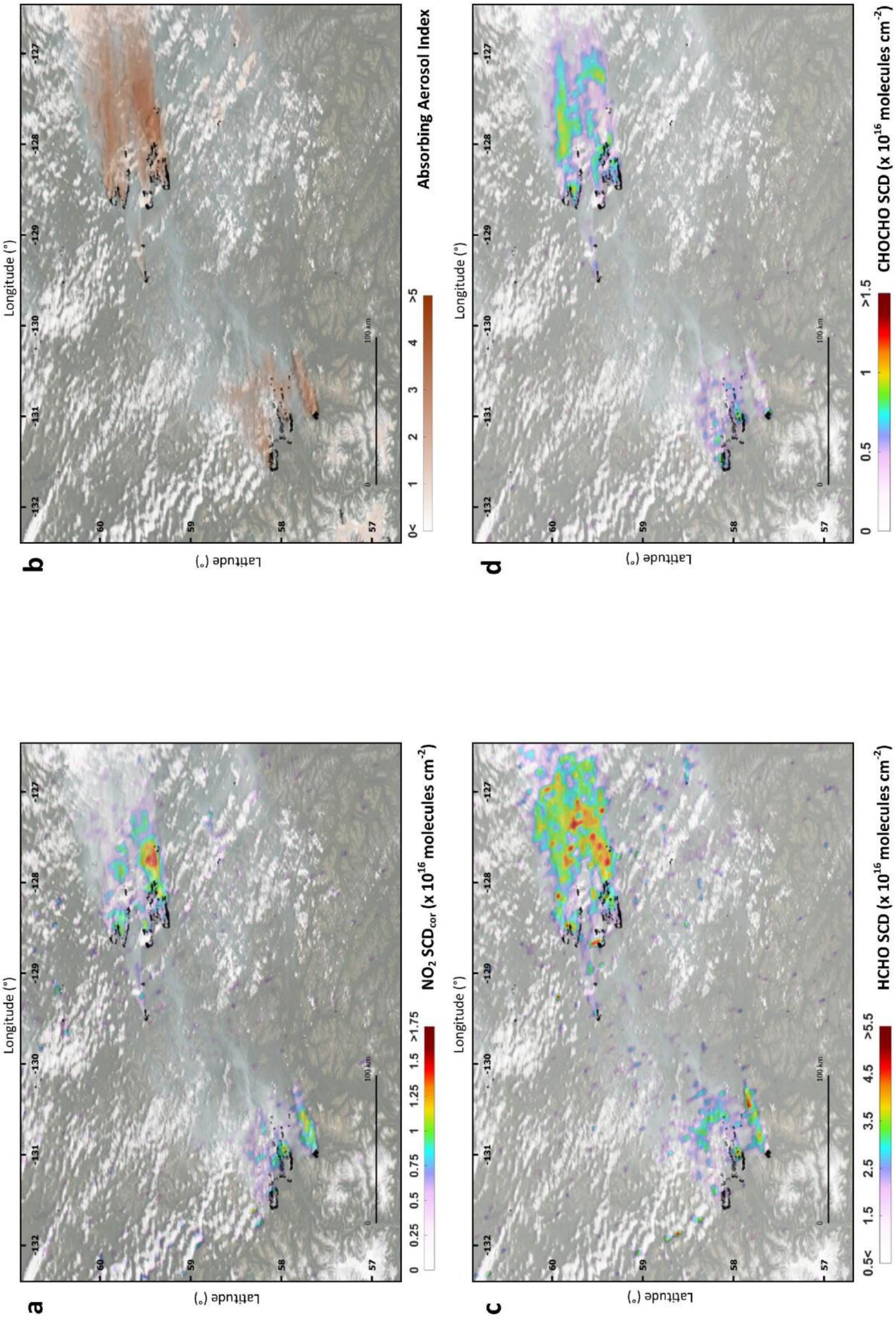
a
b
c
d
Longitude (°)
Latitude (°)
-132
-131
-130
-129
-128
-127
60
59
58
57
0
100 km
NO$_2$ SCD$_{cor}$ (x 10^{16} molecules cm^{-2})
0
0.25
0.5
0.75
1
1.25
1.5
>1.75
Absorbing Aerosol Index
0<
1
2
3
4
>5
HCHO SCD (x 10^{16} molecules cm^{-2})
0.5<
1.5
2.5
3.5
4.5
>5.5
CHOCHO SCD (x 10^{16} molecules cm^{-2})
0
0.5
1
>1.5

Supplementary Fig. 1 | Examples of TROPOMI observations of nitrogen dioxide, absorbing aerosol index, formaldehyde and glyoxal. **a**, NO_2 slant column densities (corrected for stratospheric NO_2 absorption), for British Columbia on 21 August 2018 (same as Fig. 1). NO_2 SCDs are retrieved in the same wavelength interval as HONO SCDs. **b**, Absorbing aerosol index (dimensionless) using the wavelength pair 354/388 nm. **c-d**, Formaldehyde and glyoxal slant column densities, respectively. **b-d** are for the same scene as (**a**). The background layers are true-color RGB images with fires detection and thermal anomalies product (black points) from VIIRS/Suomi-NPP instrument (source: https://worldview.earthdata.nasa.gov/), showing smoke aerosols and the fires source locations.

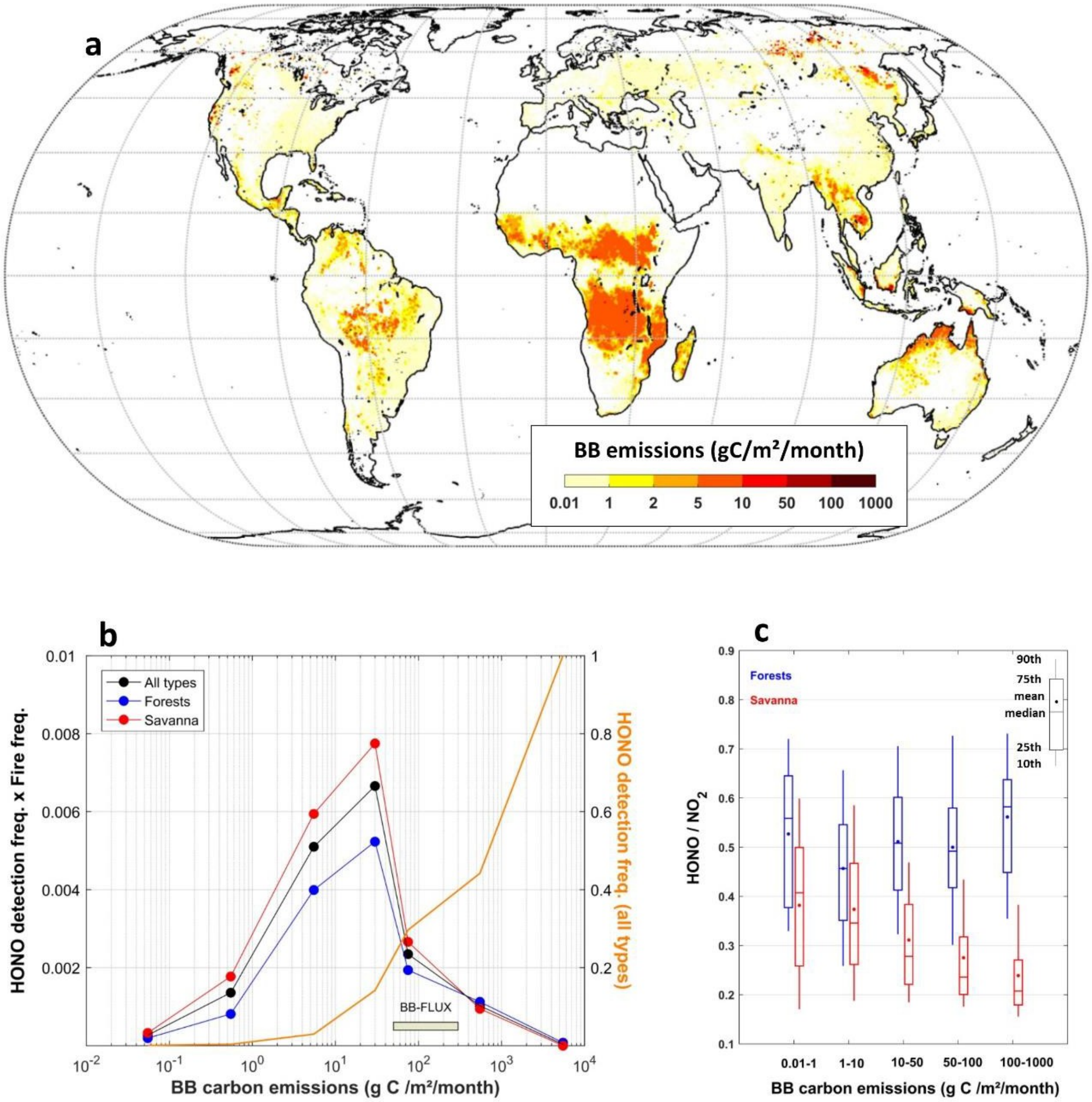

Supplementary Fig. 2 | Global biomass burning carbon emissions, and statistical analysis of TROPOMI HONO detections and HONO/NO_2 with fire activity data. **a**, Yearly averaged biomass burning carbon emissions from GFED (May 2018-April 2019). **b**, HONO detection frequency multiplied by fire frequency, per bin of carbon emission (monthly averages at 1°x1°), for savanna, forests and both biomes merged, based TROPOMI one-year measurements. HONO detections are mainly found for emissions of 0.5-500 g C/m^2/month; small agriculture fires are not observed. The HONO detection frequency (in orange, for all vegetation types) is estimated, by the fraction of the grids with at least one HONO detection, for a particulate BB carbon emission rate. The pale yellow rectangle gives an indicative range of carbon emissions for the fires during the BB-FLUX campaign. **c**, Whisker plot of RHN for bins of carbon emissions (same as (**b**)), for savanna and forest fires.

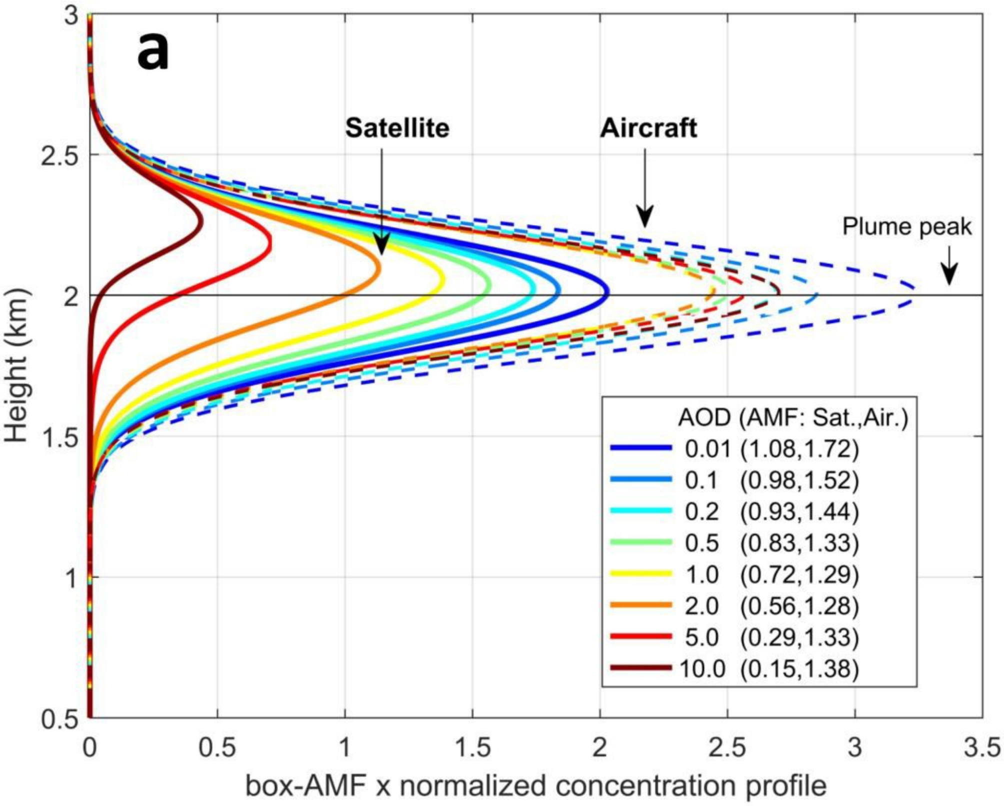
a
Satellite
Aircraft
Plume peak
Height (km)
0.5
1
1.5
2
2.5
3
0
0.5
1
1.5
2
2.5
3
3.5
box-AMF x normalized concentration profile
AOD (AMF: Sat.,Air.)
0.01 (1.08,1.72)
0.1 (0.98,1.52)
0.2 (0.93,1.44)
0.5 (0.83,1.33)
1.0 (0.72,1.29)
2.0 (0.56,1.28)
5.0 (0.29,1.33)
10.0 (0.15,1.38)

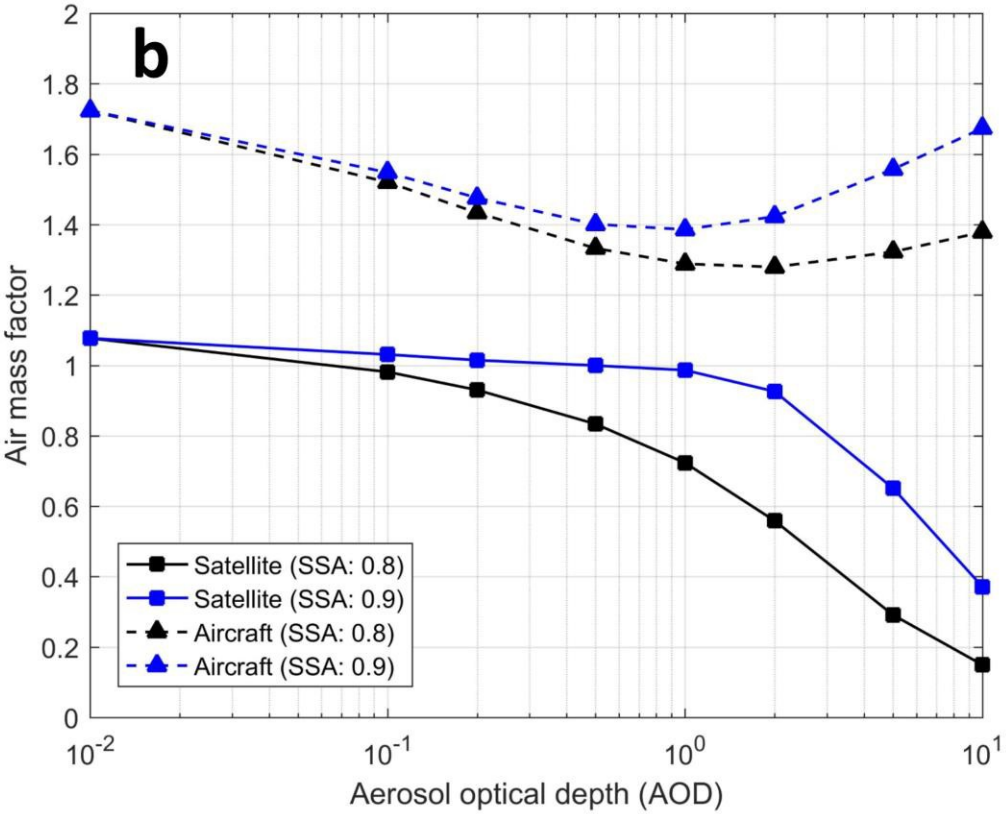
b
Air mass factor
0
0.2
0.4
0.6
0.8
1
1.2
1.4
1.6
1.8
2
10^{-2}
10^{-1}
10^{0}
10^{1}
Aerosol optical depth (AOD)
Satellite (SSA: 0.8)
Satellite (SSA: 0.9)
Aircraft (SSA: 0.8)
Aircraft (SSA: 0.9)

Supplementary Fig. 3 | Illustration of measurement sensitivity change for varying aerosol optical depth for a smoke plume peaking at 2km. a, Height-resolved contribution to the total AMF (Methods) for satellite nadir and aircraft (at 1km flying altitude) zenith-sky viewing geometries, as function of AOD. Satellite and aircraft total AMFs are in the legend. For the satellite geometry, the reduction of sensitivity and shift towards the upper-part of the plume for increasing AOD is clearly visible. Calculations are for clear-sky standard atmosphere, 30° solar zenith angle, 0.05 surface albedo, and typical fresh biomass burning absorbing aerosols with single scattering albedo (SSA) of 0.8. **b,** AMFs for satellite nadir and aircraft zenith-sky viewing geometries, for the same conditions as (**a**), with SSA of 0.8-0.9.

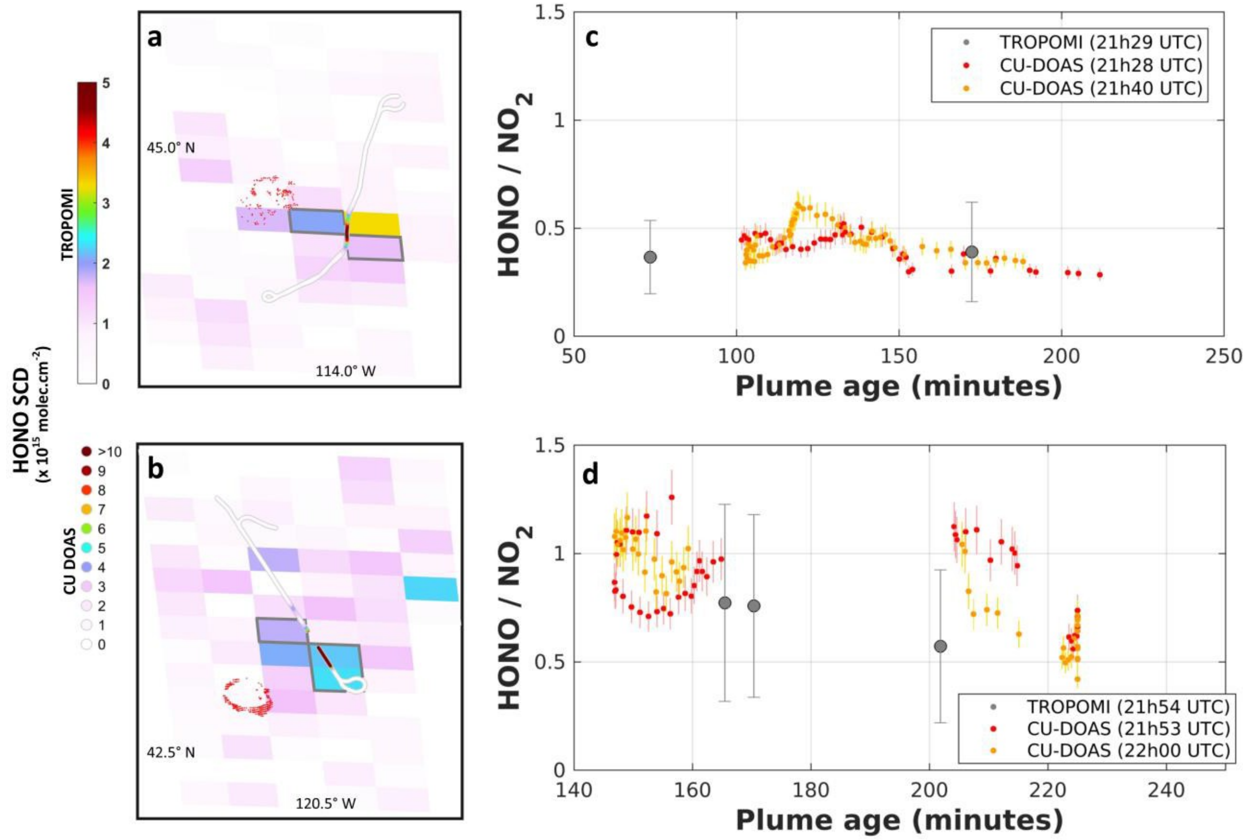

Supplementary Fig. 4 | Comparison between TROPOMI and aircraft (CU DOAS) measurements of the Rabbit Foot (Idaho) and Watson Creek (Oregon) fires on August 15 and 19, 2018. a-b, HONO slant columns from TROPOMI (rectangles) and nearly synchronized (± 15 minutes) aircraft CU-DOAS (dots), for Rabbit Foot fire (**a**) and Watson Creek fire (**b**). The fires source locations are indicated by the red points (source: https://firms.modaps.eosdis.nasa.gov/). **c-d**, Comparison between TROPOMI and aircraft RHN as function of plume age (Methods), respectively for (**a-b**). TROPOMI pixels delineated by grey lines in (**a-b**) are used for the comparison, and correspond to unambiguous detections of both HONO and NO_2 with SCDs>2xretrieval uncertainty (other pixels are considered not suitable for comparison). The two aircraft traverses of the plumes are plotted separately. Aircraft measurements more than 5 km away from the satellite pixels are not considered. Error bars correspond to systematic uncertainties on RHNs.

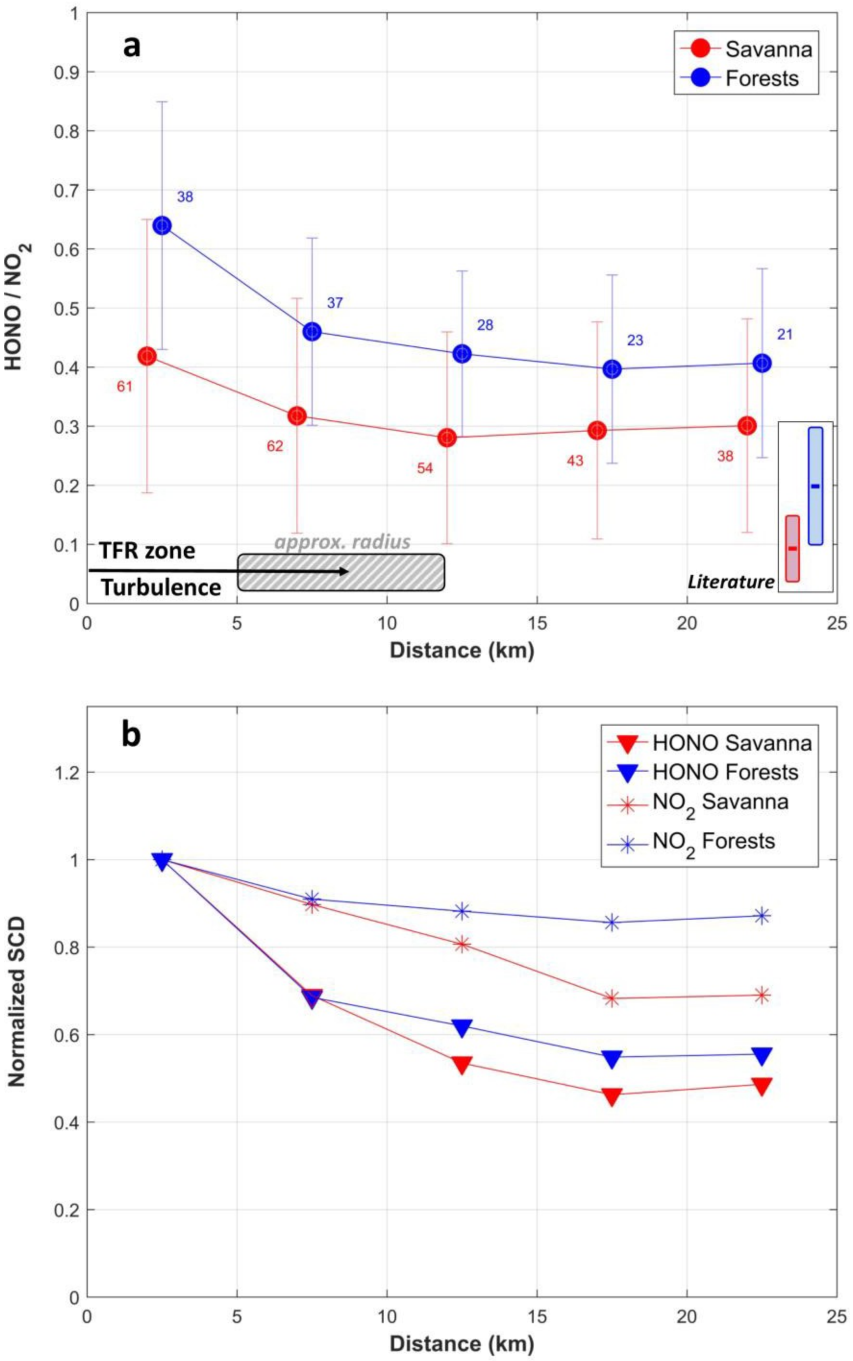

Supplementary Fig. 5 | RHN and normalized slant columns dependence with distance from HONO maximum. a, Averages of RHN for extra-tropical forest and savanna ecosystems, as a function of the distance from the measured HONO maxima for the 100 largest measured HONO SCDs. Error bars are RHN standard deviations; numbers are the total pixels per distance bin. RHN peaks are found within the 5-12 km radius of temporary flight restriction (TFR) zone or affected by fire-induced turbulence. The TROPOMI results are classified using MODIS land cover type[1]. The inset colored bars indicate the range (mean ± standard deviation) of RHN found in the literature (Supplementary Table S2, excluding fresh plumes from large wildfires[2]). **b**, same as (**a**) for the HONO and NO_2 slant column densities (normalized).

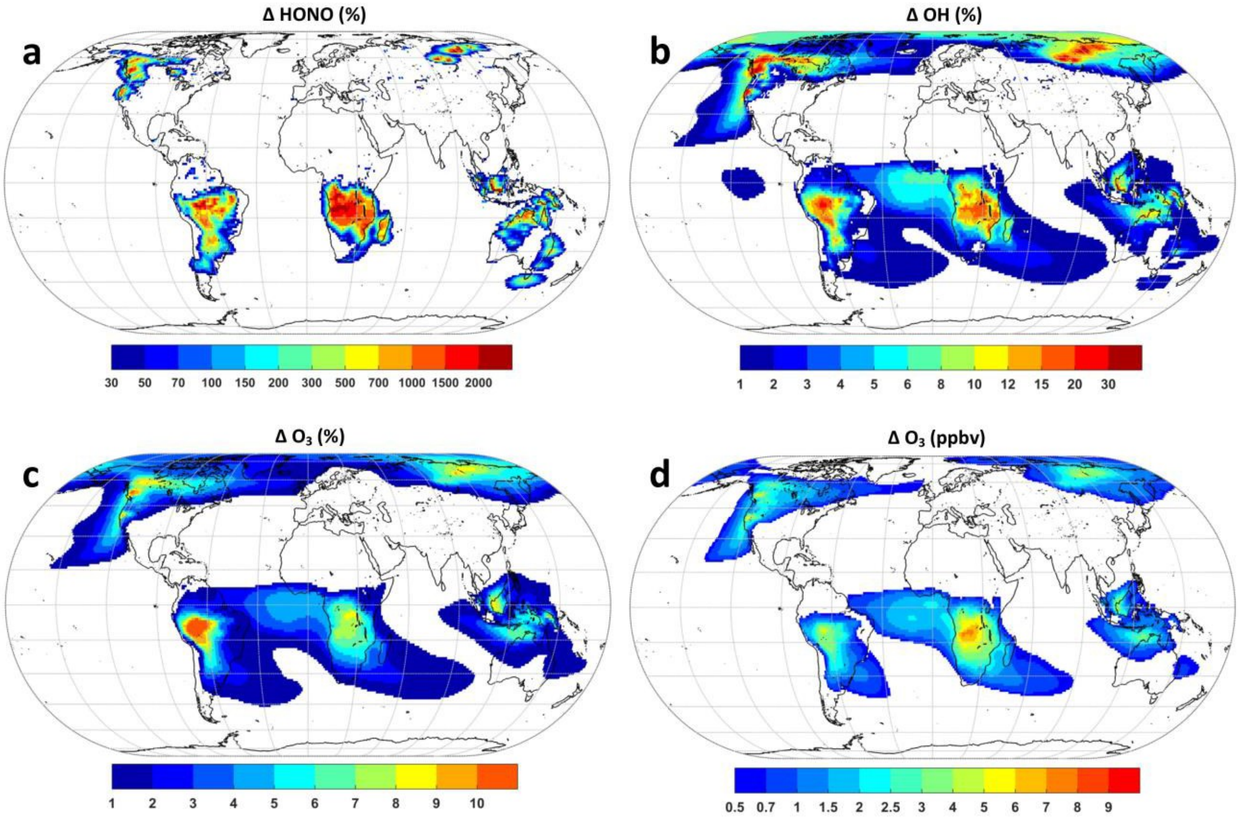

Supplementary Fig. 6 | Modelled impact of pyrogenic HONO. Calculated enhancement in the near-surface mixing ratios of HONO (a), OH (b) and O_3 (c-d) due to the inclusion of pyrogenic HONO emissions, for the month of August 2018.

Supplementary Table 1. Summary error budget of NO$_2$ SCD, HONO SCD and RHN, for satellite and aircraft measurements* used in this study.

	Satellite	Aircraft	Evaluation method - reference
NO$_2$			
Random error (molec/cm^2)	1.8x10^{15}	0.6x10^{15}	Data scatter (1-σ) in clean regions
Random error (%)	12	3	
Absorption cross-section			
Uncertainty (%)	3	3	Vandaele et al. (1998)
Temperature[⸸] dep. ± 20K (%)	4	≤4	Behrens et al. (2018)
Systematic error[§] (molec/cm^2)	1.3x10^{15}	0.9x10^{15}	Sensitivity tests
Systematic error (%)	9	4	
HONO			
Random error (molec/cm^2)	0.7x10^{15}	0.2x10^{15}	Data scatter (1-σ) in clean regions
Random error (%)	9	2	
Absorption cross-section (%)	6	6	Stutz et al. (2000), Gratien et al. (2009)
Systematic error[§] (molec/cm^2)	0.8x10^{15}	0.3x10^{15}	Sensitivity tests
Systematic error (%)	11	3	
RHN			
Random error ** (%)	21.2 (40)	5.1	Precision of single measurement
Systematic error ** (%)	26.7 (25)	10.0	Accuracy for comparison with literature
AMF cancellation (%)	1	0.2	AMF calculations over DOAS fit interval[δ]
Comparison total error (%)	25.5	6.9	Accuracy excluding cross-sections errors
Mean relative difference (%) (satellite – aircraft) ± statistical error	+6 ± 8		Figure 2c and Supplementary Figure S4 over plume age intersection

* SCD percent errors given for typical HONO SCDs of 0.75 and 1.0 x10^{16} molec/cm^2, NO$_2$ SCDs of 1.5 and 2.25 x10^{16} molec/cm^2, for satellite and aircraft observations, respectively.

** Satellite RHN errors vary depending on the observation conditions and retrieved SCDs of HONO and NO$_2$. An upper limit RHN random error is of 40% for low SCDs. A global estimate of RHN systematic error is of about 25% when accounting for the range of observed SCDs including the conditions with high NO$_2$ (savanna fires).

[δ] Radiative transfer simulations for varying aerosol optical depth and single scattering albedo (as in Supplementary Fig. S3). Vertical profile shapes of HONO and NO$_2$ taken identical.

[⸸] Difference between plume mean temperature and 294K used in DOAS spectral fitting. The effective plume temperature of the Rabbit Foot fire plume was 277 +- 2 K, and the <4% error is an upper limit.

[§] Mean values derived by varying the settings of the DOAS analysis and SCD background corrections.

Supplementary Table 2. RHNs reported in the literature and in this study, for different types of biomass burning. For each literature study, the results are given as means. The TROPOMI results are classified using MODIS land cover type[1].

	Savanna, grassland, shrubland	Tropical forest	Extra-tropical forest
Field measurements	**0.05 – 0.10**	**0.17 – 0.22**	**0.06 – 0.41 (0.86[δ])**
Trentman et al. (2005)	0.05	-	-
Burling et al. (2011)	0.10 (oak savanna)	-	0.14
Akagi et al. (2012)	-	-	0.17 (chaparral)
Akagi et al. (2013)	-	-	0.27
Bytnerowicz et al. (2016)	-	-	0.06
Müller et al. (2016)	-	-	0.21
Weise et al. (2015)	-	-	0.19
Yokelson et al. (2007)	-	0.17	-
Yokelson et al. (2009)	-	0.22	-
Yokelson et al. (2013)	-	-	0.41 (coniferous canopy)
Peng et al. (2020)	-	-	0.86
Laboratory experiments[§]	**0.05 – 0.19**	**0.17**	**0.13 – 0.20**
Burling et al. (2010)	0.05	-	0.13
Keene et al. (2006)	-	0.17	-
Selimovic et al. (2018)	-	-	0.19
Stockwell et al. (2015)	0.07	-	0.20
Yokelson et al. (2013)	0.19 (semiarid shrubland)	-	-
This study: average ± error*	**0.34±0.08**	**0.41±0.09**	**0.54±0.12**
(10th - 90th percentile)	(0.14 - 0.61)	(0.23 - 0.62)	(0.32 - 0.78)

[δ] Fresh smoke from large wildfires.

[§] NO_2 is assumed in a non-photostationary state for control burns. $HONO/NO_2$ values are calculated for $HONO/NO_x$ molar emission ratios, adapted from reported emission factors (g kg^{-1} of dry matter) of HONO and NO_x (as NO). A fixed NO_x/NO_2 ratio of 1.2 is applied to estimate $HONO/NO_2$ ratios representative of atmospheric measurements of biomass burning plumes[21].

* Systematic uncertainty

Supplementary Table 3. DOAS settings used in this study for TROPOMI retrievals of HONO, NO_2, HCHO and CHOCHO.

HONO and NO_2	
Fitting interval	337-375 nm (TROPOMI band 3)
Cross-sections	HONO 296K (Stutz et al., 2010), NO_2 294K (Vandaele et al., 1998), water vapor (Polyansky et al., 2018), O_2-O_2 293K (Thalman and Volkamer, 2013), O_3 223K and 243K (Serdyuchenko et al., 2014), BrO 223K (Fleischmann et al., 2004), HCHO 298K (Meller and Moortgat, 2000), Ring (Chance and Spurr, 1997)
Polynomial	5th order
Intensity offset	Linear, 1st order
Wavelength shift	1st order
Reference spectrum	Daily radiance (averaged per across-track position) in equatorial Pacific sector (150°E-110°W, 5°S-5°N)
Post-processing	NO_2 SCD stratospheric correction: Latitudinal parameterization (per across-track position) in clean Pacific sector (160°E-150°W)
HCHO	
Fitting interval	328.5-359 nm (TROPOMI band 3)
Cross-sections	HCHO 298K (Meller and Moortgat, 2000), NO_2 220K (Vandaele et al., 1998), O_2-O_2 293K (Thalman and Volkamer, 2013), BrO 223K (Fleischmann et al., 2004), Ring (Chance and Spurr, 1997), O_3 223K and 243K (Serdyuchenko et al., 2014) + Non-linear O_3 absorption effect: 2 pseudo-cross sections from the Taylor expansion of the wavelength and the O_3 optical depth (Puķīte et al., 2010).
Polynomial	5th order
Intensity offset	Linear, 1st order
Wavelength shift	1st order
Reference spectrum	Daily radiance (averaged per across-track position) in equatorial Pacific sector (150°E-110°W, 5°S-5°N)
CHOCHO	
Fitting interval	435-460 nm (TROPOMI band 4)

Cross-sections	CHOCHO (Volkamer et al., 2005), NO_2 220K and 294K (Vandaele et al., 1998), water vapor (Rothman et al., 2013), O_2-O_2 293K (Thalman and Volkamer, 2013), O_3 243K (Serdyuchenko et al., 2014), H_2O liquid (Mason et al., 2016), Ring (Chance and Spurr, 1997)
Polynomial	3rd order
Intensity offset	Linear, 1st order
Wavelength shift	1st order
Reference spectrum	Daily radiance (averaged per across-track position) in equatorial Pacific sector (180°E-120°W, 15°S-15°N)

Supplementary Table S4. VOC photolysis reactions considered as radical sources; OH yield Y_{OH} (assuming NO/NO_2 = 0.2 in biomass burning plumes); ratio of their photolysis rates (radical channel only) relative to that of HCHO, calculated at 30° zenith angle for 300 DU ozone; and relative uncertainty (%) on the product $Y_{OH} \times J_{VOC}$, accounting for uncertainties on the photolysis parameters, based on compilations of experimental data from JPL[32] and IUPAC[33], and on the yield of OH, assuming a 50% error in the conversion of acylperoxy radicals into OH radicals (resulting from a factor of 2 error in the NO to NO_2 ratio).

Reactions	**Y_{OH}(VOC)**	**J_{VOC}/J_{HCHO} (s^{-1} s)**	**$\sigma(Y_{OH} \times J_{VOC})$ (%)**
$HCHO \rightarrow H+HCO$	2	1.00	15
$CH_3CHO \rightarrow CH_3+CHO$	2	0.146	15
$C_2H_5CHO \rightarrow C_2H_5+CHO$	2	0.232	20
$C_3H_7CHO \rightarrow C_3H_7+CHO$	2	1.094	30
$CH_3COCH_3 \rightarrow CH_3CO+CH_3$	1.3	0.0162	27
$C_2H_5COCH_3 \rightarrow CH_3CO+C_2H_5$	1.3	0.080	60
acrolein → products	0.39	0.030	30
crotonaldehyde → products	2	0.042	30
methacrolein → products	1.51	0.061	100
methylvinylketone → $CH_3CO+CH_2{=}CH$	1.3	0.066	60
$HOCH_2CHO \rightarrow CHO+CH_2OH$	2	0.346	30
$HOCH_2COCH_3 \rightarrow CH_3CO+CH_2OH$	1.3	0.056	50
$CHOCHO \rightarrow 2\ CHO$	2	2.23	60
$CH_3COCHO \rightarrow CH_3CO+CHO$	1.3	4.13	60
$CH_3COCOCH_3 \rightarrow 2\ CH_3CO$	0.6	8.42	100
2-furfural → products	2	0.23	100

Supplementary Table S5. Alkene ozonolysis reactions considered as radical sources; OH yield; reaction rate constant at 286 K; OH production for 1 ppbv VOC at 286 K, with 50 ppbv O_3 and $[M]=1.9\times10^{19}$ molec. cm^{-3}, calculated as $P_{OH}(VOC+O_3$, in pptv $h^{-1}) = k(VOC+O_3) \times [O_3$ in molec. $cm^{-3}] \times (OH\ yield) \times 3600\times10^3$; and relative uncertainty (%) on OH production, accounting for uncertainties in the OH yield (assumed equal to 20%) and in the reaction rate constant[34]. OH production from monoterpenes + O_3 depends on speciation (see text). The large uncertainty for monoterpenes $\sigma(P_{OH}(VOC+O_3))$ allows for a factor of 3 error on α- to β-pinene ratio in fire plumes.

Reactions	**OH yield**	***k*(VOC+O$_3$)**	***P*$_{OH}$(VOC+O$_3$)**	**σ(*P*$_{OH}$(VOC+O$_3$))**
		(10^{-18} molec.$^{-1}$ cm^3 s^{-1})	**(pptv h^{-1})**	**(%)**
ethene + O_3	0.26	1.1	1	45
propene + O_3	0.92	7.7	24	55
1-butene + O_3	0.92	8.0	25	40
i-butene + O_3	1.64	9.0	50	35
trans-2-butene + O_3	1.39	160	758	45
cis-2-butene + O_3	1.39	110	521	45
butadiene + O_3	0.29	4.6	46	55
1-pentene + O_3	0.92	10	31	55
1-hexene + O_3	0.92	11	34	55
isoprene + O_3	0.56	9.6	18	35
α-pinene + O_3	1.60	86	469	55
β-pinene + O_3	0.70	16	38	55
monoterpenes + O_3			146	200

Supplementary Table 6. Molar enhancement ratios in biomass burning plumes relative to HCHO[35]. The standard error is given between parentheses, accounting for the standard deviation and number of measurements for each VOC. Those errors might be overestimated given the expected (but not quantified) correlation between Δ(VOC) and Δ(HCHO).

	Δ(VOC)/Δ(HCHO) (mol/mol)			
	savanna	**tropical forests**	**temperate forests**	**boreal forests**
CH_3CHO	0.488(0.126)	0.673(0.476)	0.367(0.059)	0.316(0.045)
C_2H_5CHO	0.022(0.016)	0.022(0.022)	0.022(0.005)	0.071(0.071)
C_3H_7CHO	0.037(0.033)	0.023(0.016)	0.022(0.006)	0.038(0.038)
CH_3COCH_3	0.198(0.029)	0.136(0.136)	0.144(0.031)	0.470(0.183)
$C_2H_5COCH_3$	0.044(0.014)	0.087(0.087)	0.046(0.014)	0.032(0.00)
acrolein	0.209(0.044)	0.145(0.145)	0.088(0.033)	0.101(0.101)
crotonaldehyde	0.087(0.087)	0.043(0.043)	0.082(0.082)	0.105(0.105)
methacrolein	0.045(0.045à	0.025(0.025)	0.027(0.016)	0.024(0.015)
methylvinylketone	0.080(0.080)	0.070(0.070)	0.034(0.010)	0.024(0.017)
$HOCH_2CHO$	0.088(0.034)	0.091(0.091)	0.097(0.097)	0.137(0.137)
$HOCH_2COCH_3$	0.185(0.057)	0.230(0.230)	0.220(0.220)	0.161(0.161)
CHOCHO	0.168(0.168)	0.129(0.129)	0.162(0.162)	0.204(0.204)
CH_3COCHO	0.136(0.096)	0.090(0.090)	0.054(0.054)	0.145(0.145)
$CH_3COCOCH_3$	0.099(0.028)	0.106(0.106)	0.149(0.064)	0.068(0.068)
2-Furfural	0.185(0.108)	0.102(0.102)	0.078(0.046)	0.109(0.109)
Ethane	0.740(0.066)	0.496(0.048)	0.577(0.035)	0.943(0.153)
propene	0.267(0.051)	0.256(0.213)	0.216(0.146)	0.273(0.254)
1-butene	0.036(0.006)	0.016(0.011)	0.031(0.005)	0.049(0.022)
i-butene	0.018(0.003)	0.024(0.024)	0.022(0.006)	0.016(0.006)
trans-2-butene	0.009(0.002)	0.007(0.005)	0.010(0.003)	0.009(0.003)
cis-2-butene	0.007(0.001)	0.007(0.005)	0.010(0.003)	0.007(0.003)

butadiene	0.043(0.007)	0.035(0.035)	0.033(0.005)	0.028(0.005)
1-pentene	0.008(0.001)	0.010(0.010)	0.010(0.002)	0.011(0.003)
1-hexene	0.012(0.002)	0.010(0.010)	0.014(0.002)	0.022(0.022)
isoprene	0.036(0.018)	0.040(0.028)	0.021(0.00)	0.019(0.019)
monoterpenes	0.019(0.008)	0.014(0.014)	0.124(0.069)	0.139(0.139)

Supplementary Table 7. Contribution of VOC photolysis reactions to the production of OH radicals, relative to that of HCHO, based on the yields and rates of Supplementary Table 4 and on the enhancement ratios of Supplementary Table 6. The estimated uncertainty is given within parentheses.

	$P_{OH}(VOC)/P_{OH}(HCHO)$ (pptv h^{-1} $pptv^{-1}$ h)			
	savanna	**tropical forests**	**temperate forests**	**boreal forests**
CH_3CHO	0.071(0.029)	0.098(0.084)	0.054(0.017)	0.046(0.013)
C_2H_5CHO	0.005(0.005)	0.005(0.006)	0.005(0.002)	0.016(0.019)
C_3H_7CHO	0.040(0.048)	0.025(0.025)	0.024(0.014)	0.042(0.055)
CH_3COCH_3	0.002(0.001)	0.001(0.001)	0.001(0.001)	0.004(0.003)
$C_2H_5COCH_3$	0.002(0.002)	0.004(0.006)	0.002(0.002)	0.002(0.001)
acrolein	0.001(0.001)	0.001(0.001)	0.001(0.001)	0.001(0.001)
crotonaldehyde	0.004(0.005)	0.002(0.003)	0.003(0.004)	0.004(0.005)
methacrolein	0.002(0.004)	0.001(0.002)	0.001(0.002)	0.001(0.002)
methylvinylketone	0.003(0.005)	0.003(0.005)	0.001(0.001)	0.001(0.001)
$HOCH_2CHO$	0.030(0.021)	0.031(0.040)	0.034(0.044)	0.047(0.061)
$HOCH_2COCH_3$	0.007(0.006)	0.008(0.012)	0.008(0.012)	0.006(0.009)
CHOCHO	0.375(0.600)	0.288(0.461)	0.361(0.578)	0.455(0.728)
CH_3COCHO	0.365(0.32)	0.242(0.387)	0.145(0.232)	0.389(0.622)
$CH_3COCOCH_3$	0.250(0.321)	0.268(0.536)	0.376(0.538)	0.172(0.344)
2-Furfural	0.043(0.068)	0.023(0.046)	0.018(0.029)	0.025(0.050)
ALL except CHOCHO	0.825(0.48)	0.71(0.67)	0.67(0.59)	0.76(0.72)

Supplementary Table 8. Contribution of VOC ozonolysis reactions to the production of OH radicals calculated for 50 ppbv O_3 at 286 K, based on the molar enhancement ratios of Supplementary Table 6, for 1 ppbv HCHO and [M]=1.9 10^{19} molec. cm^{-3}. The uncertainties (accounting for uncertainties in ozonolysis rates and yields, and in the molar enhancements in fire plumes) are given within parentheses.

	P_{OH}(VOC) (pptv h^{-1})			
	savanna	**tropical forests**	**temperate forests**	**boreal forests**
ethene	0.72(0.39)	0.49(0.27)	0.57(0.29)	0.93(0.57)
propene	6.44(.77)	6.18(8.54)	5.21(6.39)	6.59(9.76)
1-butene	0.91(0.52)	0.40(0.44)	0.78(0.44)	1.23(1.04)
i-butene	0.45(0.03)	0.61(0.82)	0.55(0.3)	0.40(0.29)
trans-2-butene	6.82(4.58)	5.31(6.18)	7.58(5.69)	6.82(5.34)
cis-2-butene	3.66(2.17)	3.66(4.26)	5.21(3.91)	3.66(3.22)
butadiene	1.95(1.39)	1.59(2.46)	1.50(1.05)	1.27(0.93)
1-pentene	0.36(0.24)	0.45(0.70)	0.45(0.34)	0.49(0.40)
1-hexene	0.28(0.20)	0.34(0.53)	0.49(0.34)	0.76(1.18)
isoprene	0.66(0.69)	0.74(0.93)	0.38(0.28)	0.34(0.53)
monoterpenes	2.80(6.78)	2.05(6.15)	18.1(46.2)	20.3(60.9)
ALL	25.1(9.9)	21.8(13.3)	40.8(47.2)	42.8(62.1)

Supplementary references

1. Friedl, M. A. et al. MODIS Collection 5 global land cover: algorithm refinements and characterization of new datasets. *Remote Sens. Environ.* **114**, 168–182 (2010).
2. Peng, Q., et al. HONO Emissions from Western U.S. Wildfires Provide Dominant Radical Source in Fresh Wildfire Smoke. *Environ. Sci. Technol*. **54**, 5954-5963 (2020).
3. Vandaele, A. C. et al. Measurements of the NO2 absorption cross section from 42 000cm−1 to 10 000cm−1 (238–1000 nm) at 220K and 294 K. *J. Quant. Spectrosc. Ra.* **59**, 171–184 (1998).
4. Behrens, L. K. et al. GOME-2A retrievals of tropospheric NO2 in different spectral ranges – influence of penetration depth. *Atmos. Meas. Tech.* **11**, 2769-2795 (2018).
5. Stutz, J. et al. UV-vis Absorption Cross-Section of Nitrous Acid. *J. Geophys. Res.* **105**, 14585–14592 (2000).
6. Gratien, A. et al. Experimental intercomparison of the absorption cross-sections of the nitrous acid (HONO) in the ultraviolet and mid-infrared spectral regions. *Journal of Quantitative Spectroscopy and Radiative Transfer.* **110**, 256-263 (2009).
7. Trentmann, J. et al. An analysis of the chemical processes in the smoke plume from a savanna fire. *J. Geophys. Res.* **110**, D12301 (2005).
8. Burling, I. R. et al. Airborne and ground-based measurements of the trace gases and particles emitted by prescribed fires in the United States. *Atmos. Chem. Phys.* **11**, 12,197–12,216 (2011).
9. Akagi, S. K. et al. Evolution of trace gases and particles emitted by a chaparral fire in California. *Atmos. Chem. Phys.* **12**, 1397-1421 (2012).
10. Akagi, S. K. et al. Measurements of reactive trace gases and variable O_3 formation rates in some South Carolina biomass burning plumes. *Atmos. Chem. Phys.* **13**, 1141-1165 (2013).
11. Bytnerowicz, A. et al. Ground-level air pollution changes during a boreal wildland mega-fire. *J. Sci. tot. Environ.* **572**, 755-769 (2016).
12. Müller, M. et al. In situ measurements and modeling of reactive trace gases in a small biomass burning plume. *Atmos. Chem. Phys.* **16**, 3813-3824 (2016).
13. Weise, D. R., Johnson, T. J., Reardon, J. Particulate and trace gas emissions from prescribed burns in southeastern U.S. fuel types: Summary of a 5-year project. *Fire Safety Journal.* **74**, 71-81 (2015).
14. Yokelson, R. J. et al. The Tropical Forest and Fire Emissions Experiment: overview and airborne fire emission factor measurements. *Atmos. Chem. Phys.* **7**, 5175-5196 (2007).
15. Yokelson, R. J. et al. Emissions from biomass burning in the Yucatan. *Atmos. Chem. Phys.* **9**, 5785–5812 (2009).
16. Yokelson, R. J. et al. Coupling field and laboratory measurements to estimate the emission factors of identified and unidentified trace gases for prescribed fires. *Atmos. Chem. Phys.* **13**, 89-116 (2013).

17. Burling, I. R. et al. Laboratory measurements of trace gas emissions from biomass burning of fuel types from the southeastern and southwestern United States. *Atmos. Chem. Phys.* **10**, 11115-11130 (2010).
18. Keene, W. C. et al. Emissions of major gaseous and particulate species during experimental burns of southern African biomass. *J. Geophys. Res.* **111**, D04301 (2006).
19. Selimovic, V. et al. Aerosol optical properties and trace gas emissions by PAX and OP-FTIR for laboratory-simulated western US wildfires during FIREX. *Atmos. Chem. Phys.* **18**, 2929-2948 (2018).
20. Stockwell, C. E., Veres, P. R., Williams, J., Yokelson, R. J. Characterization of biomass burning emissions from cooking fires, peat, crop residue, and other fuels with high-resolution proton-transfer-reaction time-of-flight mass spectrometry. *Atmos. Chem. Phys.* **15**, 845-865 (2015).
21. Simpson, I. J. et al. Boreal forest fire emissions in fresh Canadian smoke plumes: C1-C10 volatile organic compounds (VOCs), CO_2, CO, NO_2, NO, HCN and CH_3CN. *Atmos. Chem. Phys.* **11**, 6445-6463 (2011).
22. Polyansky, O. L. et al. Exomol molecular line lists XXVI: a complete high accuracy line list for water. *Mon. Not. R. Astron. Soc.* **480**(2), 2597–2608 (2018).
23. Thalman, R. M., Volkamer, R. Temperature Dependent Absorption Cross-Sections of O_2-O_2 collision pairs be- tween 340 and 630nm and at atmospherically relevant pressure. *Phys. Chem. Chem. Phys.* **15**, 15371–15381 (2013).
24. Serdyuchenko, A., Gorshelev, V., Weber, M., Chehade, W., Burrows, J. P. High spectral resolution ozone absorption cross-sections – Part 2: Temperature dependence. *Atmos. Meas. Tech.* **7**, 625–636 (2014).
25. Fleischmann, O. C., Hartmann, M., Burrows, J.P., Orphal, J. New ultraviolet absorption cross-sections of BrO at atmospheric temperatures measured by time-windowing Fourier transform spectroscopy. *J. Photochem. Photobiol. A.* **168**, 117–132 (2004).
26. Meller, R., Moortgat, G. K. Temperature dependence of the absorption cross section of HCHO between 223 and 323 K in the wavelength range 225–375 nm. *J. Geophys. Res.* **105**, 7089–7102 (2000).
27. Chance, K., Spurr, R. J. Ring effect studies: Rayleigh scattering including molecular parameters for rotational Raman scattering, and the Fraunhofer spectrum. *Appl. Optics*. **36**, 5224–5230 (1997).
28. Puķīte, J., Kühl, S., Deutschmann, T., Platt, U., Wagner, T. Extending differential optical absorption spectroscopy for limb measurements in the UV. *Atmos. Meas. Tech.* **3**, 631–653 (2010).
29. Volkamer, R., Spietz, P., Burrows, J.P., Platt, U. High-resolution absorption cross-section of glyoxal in the UV-vis and IR spectral ranges. *J. Photochem. Photobiol. A: Chemistry.* **172**(1), 35–46 (2005).
30. Rothman, L. S. et al. The HITRAN 2012 molecular spectroscopic database. *Journal of Quantitative Spectroscopy and Radiative Transfer.* **130**, 4–50 (2013).
31. Mason, J. D., Cone, M. T., Fry, E. S. Ultraviolet (250–550 nm) absorption spectrum of pure water. *Appl. Optics. Optical Society of America*, **55**(25), p. 7163. (2016).

32. Burkholder, J. B. et al. Chemical Kinetics and Photochemical Data for Use in Atmospheric Studies. Jet Propulsion Laboratory (JPL), California Institute of Technology, Pasadena, California. http://jpldataeval.jpl.nasa.gov (2015).
33. Atkinson, R. et al. Evaluated kinetic and photochemical data for atmospheric chemistry: volume I - Gas phase reactions of O_x, HO_x, NO_x, and SO_x species. *Atmos. Chem. Phys.* **4**, 1461-1738 (2004). http://iupac.pole-ether.fr/),
34. Atkinson, R. et al. Evaluated kinetic and photochemical data for atmospheric chemistry: Volume II – gas phase reactions of organic species. *Atmos. Chem. Phys.* **6**, 3625-4055 (2006).
35. Andreae, M. O. Emissions of trace gases and aerosols from biomass burning – An updated assessment. *Atmos. Chem. Phys.* **19***,* 8523-8546 (2019).